PCCP

Accepted Manuscript

ROYAL SOCIETY OF CHEMISTRY

www.rsc.org/pccp

From Lime to Silica and Alumina:

Systematic Modeling of Cement Clinkers using a General Force-Field

A. A. Freitas[1,2], R. L. Santos[1,2], R. Colaço[2,3], R. Bayão Horta[3], J. N. Canongia Lopes*[,2,3]

[1]CIMPOR - Cimentos de Portugal, SGPS S.A., Rua Alexandre Herculano, 35, 1250-009 Lisboa, Portugal

[2]Centro de Química Estrutural, [3]Instituto Superior Técnico, University of Lisbon, Av. Rovisco Pais, 1049-001 Lisboa, Portugal

*Phone (+351) 218419261. E-mail: jnlopes@ist.utl.pt

Abstract

Thirteen different cement-clinker crystalline phases present in the lime-silica-alumina system have been systematically modeled using a simple and general force field. This constitutes a new kind of approach to the study of lime-silica-alumina systems, where the simpler and more transferable Lennard-Jones potential is used instead of the more traditional Buckingham potential. The results were validated using experimental density and structural data. Elastic properties were also considered. Six amorphous phases (corresponding to calcium/silicon ratios corresponding to belite, rankinite, wollastonite and alumina-doped amorphous wollastonite with 5, 10 and 15% alumina content) were also studied using Molecular Dynamics simulations. The obtained MD trajectories were used to characterize the different crystalline and amorphous phases in terms of the corresponding radial distribution functions, aggregate analyses and connectivity among silica groups. These studies allowed the direct comparison between crystalline and amorphous phases and revealed how the structure of the silica network is modified in amorphous materials or by the inclusion of other structural units such as alumina. The knowledge at an atomistic level of such modifications is paramount for the formulation of new cement-clinker phases.

Keywords: Molecular Dynamics, Cement Clinker, Belite, Rankinite, Wollastonite

Introduction

Cement is one of the most used materials worldwide. Ordinary Portland cement (OPC), the most commonly used cement, is made by heating a mixture of limestone (or other sources rich in calcium oxide) and clay (or other silicate sources) up to temperatures of around 1500 ºC in order to obtain a calcium-silicon oxide matrix comprising different crystalline and amorphous phases. The reaction of the cement clinker thus formed with water yields the formation of portlandite (calcium hydroxide, $Ca(OH)_2$) and of an amorphous hydration product, the so-called C-S-H gel. While portlandite introduces weakness in mortar and concrete due to its vulnerability to sulfate and carbonate attacks, the formed CSH gel ensures the strength and durability of cement stone and confers its outstanding mechanical and chemical properties.[1,2]

Given the extensive use of cement worldwide and the difficulty of transporting it, many different local sources have been used to produce clinkers with different characteristics. However, the presence of alite (tricalcium silicate, C_3S) and belite (dicalcium silicate, C_2S) as the two major phases present in Portland cement clinkers is deemed essential for the formulation of cements with good strength-development characteristics. (Hereafter we will use the cement industry nomenclature, i.e., C=CaO, S=SiO_2 and H=H_2O and A=Al_2O_3). Calcium aluminates are also present as secondary phases and can also play a role in the reactivity of the clinkers with water and the development of the mechanical properties of the cement pastes.[2]

The production of cement has a negative carbon footprint, accounting for 5% of all man-made carbon dioxide emissions. One way to reduce such footprint is to obtain suitable clinkers using lower temperatures in the calcination process and/or using clinker formulations with a lower calcium/silicon (C/S) ratio. In fact, reducing the calcium

content of cement clinkers would solve several issues simultaneously: i) limestone (calcium carbonate) is the preferred source of calcium oxide —this means that for every mole of calcium incorporated in the clinker, one mole of carbon dioxide is produced and released; ii) belite (C/S=2) can be produced at lower temperatures than alite (C/S=3); iii) rankinite (C/S=1.5) and wollastonite (C/S=1) are other calcium-silicon oxides with favorable C/S ratios and relatively low formation temperatures; iii) the C-S-H gel that is produced during the hydration process of the clinker has C/S ratios around 1.0-1.4, which means that part of the calcium present in alite clinkers is unnecessary to produce the C-S-H binder, and is released as a calcium hydroxide by-product (portlandite).

Unfortunately belite-rich clinkers are not as reactive with water as their alite-rich counterparts. However, the search for forms of belite or other calcium-silicon oxide phases, with low C/S ratios, presenting improved reactivity towards water can now be assisted using atomistic simulation techniques. In this paper we introduce a general and simple force-field parameterization that allows the systematic modeling of different cement clinkers, from lime-rich alite forms to silica-rich wollastonite phases. Unlike previous (more sophisticated) force-field parameterizations that concentrated on specific crystalline forms found on limited regions of the CaO-SiO_2 system, the present (more general) force field also describes amorphous phases and encompasses calcium-aluminum oxides and calcium-aluminum-silicon oxides.

Computational Details

All the molecular dynamics (MD) simulations were carried out with DL_POLY 2.20 code. Buckingham partial charge pair potentials for Si, O and Ca were taken from Cormack and Du[3] and the pair potential parameters for Al-O were based on those from Thomas et al.[4]

The Buckingham pair potential has the form:

$$U_{ij}(r_{ij}) = \frac{q_i q_j}{4\pi\varepsilon_0 r_{ij}} + A_{ij}\exp\left(\frac{-r_{ij}}{\rho_{ij}}\right) - \frac{C_{ij}}{r_{ij}^6} \quad (1)$$

where q_i, q_j, are the partial charges placed in atoms of type *i* and *j*, ε_0 is the permittivity of a vacuum, r_{ij} is the interatomic distance, and A_{ij}, ρ_{ij} and C_{ij} are parameters describing pair interatomic interactions. The three terms on the right-side of equation 1 represent electrostatic, repulsive and dispersive non-bonded interactions, respectively.

In the limit at the interatomic distance r_{ij} = 0 the energy given by the Buckingham potential tend to a negative infinity, which could be an issue in terms of MD simulations for systems at very high temperatures (although that is not generally the case for the temperatures discussed in this work). To overcome this potential problem, we retained the partial charges unchanged and transcribed the other non-bonded interactions parameters in order to fit a Lennard-Jones potential form (equation 2).

$$U_{ij}(r_{ij}) = \frac{q_i q_j}{4\pi\varepsilon_0 r_{ij}} + 4\varepsilon_{ij}\left(\left(\frac{\sigma_{ij}}{r_{ij}}\right)^{12} - \left(\frac{\sigma_{ij}}{r_{ij}}\right)^{6}\right) \quad (2)$$

where ε_{ij} and σ_{ij} are Lennard Jones pair interaction parameters. The fitting was performed taking into account the position of the Buckingham potential minimum at the interatomic equilibrium distance and the interatomic distance at null interatomic potential. Averages between values obtained for different types of clinker phase were considered in order to obtain the final, general parameters.

All parameters are given in Table 1. The validation of the Lennard-Jones parameters was carried out through the simulation of a series of crystals at ambient pressure and temperature and the validation of the obtained results using available experimental data.

Table 1. Interatomic potential parameters (eqns. 1 and 2) employed in this study.

	Coulomb	Buckingham			Lennard-Jones	
i-*j* pair	q_i / e	A_{ij} / eV	ρ_{ij} / Å	C_{ij} / eV.Å^{-6}	ε_{ij} / eV	σ_{ij} / Å
Si–O	2.4	18003.8	0.20520	133.54	1.16692	1.4988
Ca–O	1.2	131400.0	0.18750	60.00	0.08404	2.4203
O–O	-1.2	1388.8	0.36232	175.00	0.01407	3.2528
Ca–Ca	1.2	10000.0	0.23000	0.00	0.00011	4.1978
Al–O[a]	1.8	12201.0	0.19560	31.99	-	-
Al–O[b]	1.8	12201.0	0.19060	31.99	0.17282	1.7773

[a] Reference 4; [b] this work

The information used to generate the simulation boxes of the crystals were obtained from The American Mineralogist Crystal Structure Database.[5] The unit cells were replicated to give a simulation box with a minimum side of 5.0 nm (the size of the equilibrated simulation boxes is given in Table 2, along with the simulated structural data, cf. Results and Discussion section). Periodic boundary conditions were applied in all directions. The modeling of the crystals used a Berendsen NσT ensemble at 300 K and p = 1 atm (relaxation times of 2 ps and 0.8 ps for thermostat and barostat, respectively), timestep of 1 fs, cutoff of 1.203 nm, total simulation time of 235 ps and trajectories stored in the last 150 ps of the simulation runs (sampled at every 100 fs). The Coulomb potential was evaluated using the Ewald sum method with precision of 10^{-5}.

The simulation of the amorphous materials was adapted from reference 6. The first stage consisted in the production of a random distribution of the atoms at the desired

composition in a cubic box with sides of ca. 5.1 nm. The density was set to the corresponding room-temperature experimental value of the calcium silicate glasses.[7] The box was then pre-equilibrated under constant NVT conditions with a thermal bath of 4000 K for just 85 ps and timestep of 0.5 fs, using a Nosé-Hoover thermostat with time constant of 0.5 ps. The second stage was a run at 4000 K for another 85 ps and timestep of 1 fs, also in NVT. The third stage consisted in a run at 2500 K in NVT. To improve the statistics, at this stage five different configurations for each amorphous sample were made, all consisting in simulation runs varying between 170 ps (1 fs timestep) and 340 ps (2 fs timestep). The next stage corresponded to a temperature quench of the simulation box from 2500 K to 300 K at a rate of 10 $K.ps^{-1}$, which is typical for MD studies of glasses.[6,8] In the fifth stage the box were allowed to relax under NpT conditions for 200 ps and timestep of 2 fs at 300 K, employing a Nosé-Hoover ensemble with relaxation times of 0.5 ps and 2 ps for thermostat and barostat, respectively. The last stage consisted in a run of 50 ps with a timestep of 1 fs for data production, where the trajectories were sampled at every 100 fs. In all stages the Coulomb potential was evaluated using the Ewald sum method with precision of 10^{-5}.

The validation of the force field also included the estimation of different relevant elastic properties of the CSA materials (both crystalline and amorphous). Those properties were calculated using the linear relationship between stress σ_i and strain ε_j (Hooke's law):[9]

$$\sigma_i = \sum_{j=1}^{6} c_{ij}\varepsilon_j \quad (1)$$

where c_{ij} are the elastic stiffness coefficients of the matrix $\boldsymbol{c}$. The equation 1 can be written as:

$$\begin{bmatrix}\sigma_1\\ \sigma_2\\ \sigma_3\\ \sigma_4\\ \sigma_5\\ \sigma_6\end{bmatrix} = \begin{bmatrix} c_{11} & c_{12} & c_{13} & c_{14} & c_{15} & c_{16} \\ & c_{22} & c_{23} & c_{24} & c_{25} & c_{26} \\ & & c_{33} & c_{34} & c_{35} & c_{36} \\ & & & c_{44} & c_{45} & c_{46} \\ & symm & & & c_{55} & c_{56} \\ & & & & & c_{66} \end{bmatrix} \begin{bmatrix}\epsilon_1\\ \epsilon_2\\ \epsilon_3\\ \frac{1}{2}\epsilon_4\\ \frac{1}{2}\epsilon_5\\ \frac{1}{2}\epsilon_6\end{bmatrix} \quad (2)$$

Thus, the stress tensors were obtained from MD simulations of a series of NVT ensembles. The strains were applied in steps of 0.1% both for contraction and expansion of the lattice box (negative and positive strains, respectively) and the atomic positions were relaxed at T = 300 K. In each simulation series all but one strain was kept constant. For crystals with cubic symmetry such as C_3A, there are only three independent elastic constants, c_{11}, c_{12} and c_{44}, which can be obtained from two simulation series changing the strains ϵ_1 and ϵ_4, for example.[10] In fact for the systems simulated here the corresponding stiffness matrix was constructed applying all the six strains to the simulation boxes and the symmetric off-diagonal coefficients of the matrix ***c*** were averaged.

The elastic compliance matrix was computed from the inverse of the elastic stiffness matrix:

$$[s] = [c]^{-1} \quad (3)$$

The Voight, Reuss and Hill definitions for Bulk (K) and Shear (G) moduli are:[11]

$$K_{Voight} = \frac{(c_{11}+c_{22}+c_{33})+2(c_{12}+c_{13}+c_{23})}{9} \quad (4)$$

$$K_{Reuss} = \frac{1}{(s_{11}+s_{22}+s_{33})+2(s_{12}+s_{13}+s_{23})} \quad (5)$$

$$K = \frac{K_{Voight}+K_{Reuss}}{2} \quad (6)$$

$$G_{Voight} = \frac{(c_{11}+c_{22}+c_{33}-c_{12}-c_{13}-c_{23})+3(c_{44}+c_{55}+c_{66})}{15} \quad (7)$$

$$G_{Reuss} = \frac{15}{4(s_{11}+s_{22}+s_{33}-s_{12}-s_{13}-s_{23})+3(s_{44}+s_{55}+s_{66})} \quad (8)$$

$$G = \frac{G_{Voight}+G_{Reuss}}{2} \quad (9)$$

The Young modulus (E) and the Poisson ratio (ν) for isotropic materials were calculated from the relationships:

$$E = \frac{9KG}{3K+G} \quad (10)$$

$$\nu = \frac{c_{12}}{c_{11}+c_{12}} = \frac{3K-2G}{2(3K+G)} \quad (11)$$

Also, the coefficients of the compliance matrix s_{11}, s_{22} and s_{33} are related with the Young moduli measured along each crystallographic direction:

$$E_x = \frac{1}{s_{11}} \qquad E_y = \frac{1}{s_{22}} \qquad E_z = \frac{1}{s_{33}} \quad (12)$$

The Bulk modulus was also calculated through $P \times V$ relationships (P varying up to 3000 atm) with Buckingham and Lennard-Jones force fields for crystalline phases with known values of K.

Radial Distribution Functions $g(r_{ij})$ between representative atom pairs, coordination numbers N_{ij} and aggregation analyses of SiO_4 groups in amorphous clinker phases are presented and discussed bellow.

The ring statistics were calculated using the R.I.N.G.S. v1.2.4 code.[12] Rings containing up to 30 atoms (Si + O) were examined by the shortest-paths criterion,[13] excluding homopolar bonds (Si-Si or O-O) from the search. The cutoff distance for the Si-O bond was set to 0.19 nm in all glasses studied.

The drawings of the simulation boxes showing the coordination polyhedra were produced with the VESTA software.[14]

Results and Discussion

A systematic force-field for cement clinker sub-phases: development and rationale.

There is a large number of available force-field potential parameterizations capable of modeling materials related to cement clinkers, silicate or aluminate glasses, zeolites or other hydrated multi-component mineral systems. Some of these potentials have been built to describe the interactions between different types of atoms within a given crystal which means that the transferability of the corresponding parameters is generally not possible when considering other (analogous) systems. Historically, most of the potentials used to model cement clinker phases (and even the corresponding hydrated systems) have been based on Buckingham-type potentials,[3,4,15-21] some originally developed for silicates and alumino-silicate materials, where different three-body interaction terms are generally introduced to account for the bond-hybridization around particular atom types such as silicon and oxygen.[17] Polarizability effects can also be taken into account by using core-shell approaches instead of relying on fixed partial-charge models. Reactive MD simulations can be introduced using the appropriate reactive force-fields (e.g. ReaxFF).[22]

The rationale behind the definition of the present force field is different: instead of relying on a sophisticated model that describes with great accuracy a given crystalline structure and the modifications that can occur when such structure is subjected to different types of stress such as dislocations, defects, free surfaces, or even chemical reaction, we wanted to check how far we could go with a very simple and general force filed model in the prediction of the basic structural features of a series of different phases present in cement clinkers, thus covering both crystalline and amorphous systems present in distinct regions of the lime-silica and lime-alumina phase diagrams.

Table 2 compares different force field parameterizations considered in the present work. Some of these were tested in terms of their possible use in the construction of a general and transferable model; others are just presented and discussed due to their current relevance in the modeling of cement phases and related systems. It must be stressed that the table is by no means exhaustive —this is not a revision article.

Table 2. Summary of the force field parameterizations discussed in this work.

Ref.	Force field type	Systems / Application
Tested and used in the development of a transferable model		
3	Buckingham potential with fixed partial charges.	Soda-lime-silicate glasses. Transferable to clinker phases with 1.0 to 3.0 C/S ratios.
4	Buckingham potential with fixed partial charges.	Lime-alumina glasses (C/A = 1.67). Partially transferable to clinker phases with 0.5 to 3 C/A ratios.
This work	Buckingham and Lennard-Jones (LJ) potentials with fixed partial charges.	Transferable among different clinker phases (crystalline and amorphous) within the lime-silica-alumina ternary phase diagram.
Tested and not used in the development of a transferable model		
23	LJ potential with fixed partial charges and three-body terms.	Used for tricalcium silicate (alite). Not transferable to wollastonite.
24	Born-Mayer-Huggins potential. Fixed formal charges.	Used for molten $CaAl_2Si_2O_8$ (plagioclase). Not transferable to rankinite and wollastonite.
15	Buckingham potential with core-shell charges and three-body terms.	Used for chabazite zeolite. Transferable to rankinite but not to wollastonite.
Other relevant, state-of-the-art force fields		
25	CLAYFF: SPC-water and LJ models with fixed partial charges and three-body terms.	Calcium hydroxide (portlandite) and hydroxide or oxyhydroxide clay phases. Centered on hydroxylated systems.
26	INTEFACE FF: LJ potential with fixed partial charges.	Tricalcium silicate (alite), tricalcium aluminate, ettringite, tobermorites. Work in progress.
16	Buckingham, LJ and Morse potentials with core-shell charges.	Calcium silicate (wollastonite). Restricted to one calcium-silicate.
18	Buckingham model with three-body terms and core-shell charges.	Doped tri- and dicalcium silicates (alite and belite). Focuses on the two major cement clinker components.
17	Buckingham and LJ models with three-body terms and core-shell charges.	Calcium silicate hydrate (C-S-H gel). Tobermorite, jennite, portlandite. Focuses on cement pastes.
19	REAX FF: reactive MD simulations using the previous model.	Calcium silicate hydrate (C-S-H gel). The reactions of confined water in C-S-H.
20	Buckingham potential with fixed partial charges.	Lime, silicates. Glassy materials from quenching of melts. Centered on glasses.

The present force field generalizes and simplifies the state-of-the-art force fields usually used to model cement clinker and pastes[16-20] in three important ways: i) non-bonded interactions (repulsive contacts and dispersive) are modeled via the Lennard-Jones

potential instead of the Buckingham potential usually employed for minerals; ii) only pair potentials are considered (no three-body terms are included); iii) fixed partial charges are used instead of core-shell models.

The crucial difference between the Buckingham and Lennard-Jones potentials —Eqns. (1) and (2), respectively— lies in the description of the repulsive term corresponding to the forces that avoid the overlap of the interacting particles and maintain the atoms at the correct contact distances. In the case of the Buckingham potential those interactions are modeled via two parameters (A_{ij}, ρ_{ij}) independently from the dispersion term (parameterized via C_{ij}). On the other hand, the Lennard-Jones potential only requires two parameters that model the intensity of the dispersion forces (ε_{ij}) and the contact distance (σ_{ij}) in an interconnected way. This means that inorganic crystalline phases have been traditionally modeled using the Buckingham potential due to its superior ability for the description of the contact repulsions (packing) between atomic interaction centers. However, if the aim is to obtain a more general force-field that is able to model different crystalline and amorphous phases (where the environment and packing of a given atom type will vary from system to system), the enhanced description of a particular system awarded by the Buckingham potential can be traded-off for a larger scope of application and a higher compatibility/transferability of parameters given by the Lennard-Jones potential. In fact that has been the rationale behind the development of a very recent general force-field to be applicable at the interface between (bio)organic and inorganic systems and circumvent prevailing roadblocks that exist between the two modeling realms.[21,26,27] In the present case we will not go as far as such organic-inorganic

interfaces but will focus our efforts in the different phases present in cement clinkers and pastes.

One important issue of the transition from Buckingham to Lennard-Jones potentials is that the latter rely heavily on combination rules to obtain cross interaction parameters. Due to the close packing of atoms that is the norm in inorganic crystalline systems such rules usually yield values that need to be adjusted using extra correction parameters. In order to avoid such situation we have decided to perform the transcription of parameters between the Buckingham and Lennard-Jones potentials not only for interactions between atoms of the same type but also for the cross interactions between distinct atom types. Part of the general behavior of the Lennard-Jones potential is lost when this option is implemented but that is the price to pay for extending its applicability to inorganic crystalline systems.

The second simplification to be addressed is the absence of three-body potentials. These are deemed necessary when the interactions between certain types of atom (e.g. silicon and oxygen in silicates) have a certain covalent character and thus depend on issues such as the underlying hybridization of atomic orbitals to yield proto-molecular structures (e.g. the oxygen tetrahedra surrounding the silicon atoms). In fact for molecular species, such as those prevalent in organic systems, the so-called bonded interactions play a central role in the building of the molecular frameworks and are described using a series of two, three and four-center terms related to the molecular internal modes of motion (stretching, bending and torsion modes). For inorganic systems based on atomic species part of the covalent character of a given interaction can be associated to a charge transfer process between the two atoms in question. In such cases partial (reduced) charges have been

employed instead of the formal charges attributed to a given atomic ion. In those conditions it was found[3] that three-body terms are not strictly necessary. The exclusion of such terms have an impact not only on the speed of the simulations but also on the transferability and scope of application of the force fields: force fields with three-body terms (based on the Buckingham[15] and Lennard-Jones[23] potentials) yield very precise results for the original target systems but very poor results when applied to other (not so dissimilar) systems; force fields with fixed partial charges and no three-body terms yield acceptable structural results for a much broader array of systems (cf. next section).

The final simplification is related to the introduction of polarization effects via the use of core-shell models instead of fixed partial charges. These effects can be important (and not negligible) if one considers for instance the dielectric properties of materials, or if one is studying surfaces or defective (doped) crystals. If one is mainly focused on modeling the structural properties of bulk materials, including amorphous systems that can be obtained by quenching the corresponding mineral melts, then the use of a rigid ionic model has obvious advantages, both in terms of the required MD simulation time steps but also of transferability (the tested core-shell potential[15] yielded very poor results outside its original applicability boundaries, cf. Table 2). It must be stressed however that the use of a core-shell model in the present force field can always be re-introduced at a later stage if for instance the simulation conditions call for it (e.g. if one tries to generate a free surface from an equilibrated bulk phase).

Evaluation of the Lennard-Jones interatomic potential parameters.

The transcription of the original Buckingham interatomic potential parameters to a Lennard-Jones potential form was carried out and validated through the MD simulation of thirteen crystals at ambient pressure and temperature. Some of the selected structures represent the major components of the crystalline phases of the Ordinary Portland Cement (OPC) clinker or are additives commonly found in cements (Figure 1). Table 3 compares the experimental unit cell parameters of the thirteen crystalline structures with the respective MD values calculated employing the Lennard-Jones interatomic potentials. The calculated lattice constants are in reasonable agreement with the experimental data, even for the mayenite crystal (the major component of calcium aluminate cements) in which the framework is partially occupied by oxygen atoms.[37] Table S1 in the Electronic Supporting Information (ESI) shows the results calculated with the original Buckingham parameters. The comparison between Tables 3 and S1 attests the validity of the Buckingham to Lennard-Jones transcription process.

Table 4 compares MD and crystallographic data relative to the interatomic distances within the nine distinct studied crystalline structures (data for different polymorphs of the same type of crystal are condensed in the form of distance ranges). The agreement between the two sets of data is reasonable given the general character of the force field under discussion. For instance, the particularly difficult case of Ca-Ca distances —where the atoms can be distributed within the crystal lattices at diverse distances— is still adequately modeled by the use of common parameters for each type of atom: the unusually large Ca-Ca distance in Grossite (0.434 nm instead of 0.347-0.375 for all other crystals) is captured in the structures modeled by MD (0.450 nm instead of 0.330-0.370 for all other structures).

In Table 5 the experimental densities of four CAS glasses are compared with the corresponding MD results, along with the MD result for an amorphous material with C/S ratio equivalent to the belite crystal. These amorphous materials were selected because they have chemical compositions equivalent to some of the crystalline phases simulated and they are inside or at the boundaries of the region of interest in the CAS ternary diagram. Also, some of the selected glasses have known experimental elastic properties, allowing inspection not just of the equilibrium structural parameters but also parameters such as the bulk modulus, which involves deviation from equilibrium.

Table 6 does the same sort of distance comparison as in Table 4, but for three $(CaO)_x(SiO_2)_{1-x}$ glass models. The analyses are focused on the Si-O and Ca-O distances and are supplemented by data showing the average oxygen and calcium coordination numbers to either silicon and/or calcium. The presented results are consistent with those reported by Mead et al.,[6] namely for the C/S = 1 ratio (cf. fourth data row of Table 6). The apparent discrepancy in the coordination numbers of bridging and nonbridging oxygen atoms (O_b and O_{nb}) lies in the fact that i) their analyses are based on population analyses obtained directly from the corresponding Si-O or Ca-O radial distribution functions, while ours is performed using aggregation analyses with selected distance criteria; ii) their analyses do not take into account the possibility of free oxygen atoms (O_i, not coordinated to any silicon atom). If the type of analysis performed by Mead et al.[6] is performed on RDFs obtained directly from our MD trajectories, we obtain results very similar to theirs (cf. fifth data row of Table 6).

The validation in terms of distances and nearest neighbors for eight $(CaO)_x(SiO_2)_y(Al_2O_3)_z$ glass models is given in Table 7. The first three lines in the table

summarize the results for amorphous materials with C/S = 1.5, the lines four to six include MD data to glasses with C/S = 1.0, and the seventh and eighth rows give the results for glass models with the same chemical composition of crystalline anorthite (CAS_2) and krotite (CA), respectively. The interatomic distances Al-O and Ca-O calculated for CA are in good agreement with the experimental values of r_{AlO} = 0.176 nm and r_{CaO} = 0.238 nm found by neutron and x-ray diffraction.[51] The distances r_{AlO} and r_{SiO} of the amorphous with composition equivalent to that of anorthite are corroborated by the experimental data[48] found by energy dispersive x-ray diffraction (r_{AlO} = 0.1722 nm and r_{SiO} = 0.1647 nm). In general, the coordination numbers calculated for AlO and SiO pairs in CAS system are in line with the values found either by MD or experimentally (N_{AlO} = 4.0 in krotite-equivalent amorphous[51] and other CA glasses with composition close to eutetic,[4] $N_{AlO/SiO}$ = 3.9 in anorthite-like and other amorphous[48] in CAS system). On the other hand, the coordination number for CaO pair found in literature are much broader, once it is subject to interferences in the fitting procedure given overlap with the OO pair distribution functions, uncertainties in x-ray beam energy calibration or proper definition of the first minimum in CaO pair distribution functions in MD calculations (which effectively defines the first coordination shell). The values found for N_{CaO} range from 5.6 for krotite-like amorphous,[51] 5.59 and 6.2 by x-ray difraction[48] and MD simulation,[4] respectively, in $(CaO)_{0.63}(Al_2O_3)_{0.37}$ eutectic composition glass.

The calculated occurrence of five-fold coordinated aluminum $^{[5]}$Al (network modifier) was $^{[5]}$Al = 0.15% for glassy CAS_2 and $^{[5]}$Al = 0.05% for amorphous CA, lower than the values found by NMR[52] ($^{[5]}$Al = 7% for CAS_2 and $^{[5]}$Al = 4% for CA). The presence of oxygen triclusters μ_3 (O atoms coordinated by three Al atoms) calculated for anorthite-

like (μ_3 ~7%) and krotite-like (μ_3 ~12%) amorphous compositions are in fair agreement with the reported data (μ_3 = 1–2% for CAS_2 glass[53] and μ_3 ~5% for CA glass[54,55]). The fraction of non-bridging oxygen atoms (NBO) was calculated in 8% and 12% for CAS_2 and CA glasses, respectively, and are close to NBO = 5% determined for CAS_2 amorphous by NMR[53] and NBO = 12% found for CA glass by MD simulations.[56]

It was also confirmed that the Al distribution in simulated CAS glasses follows the Loewenstein's rule (or Al avoidance principle, valid for low Al content). The probability $P_{n,m}$ of finding SiO_4 tetrahedral units bonded to other n SiO_4 or m AlO_4 tetrahedral sites, $Q^n(m\text{Al})$, can be carried out by the following distribution:[57]

$$P_{n,m} = \frac{n!}{m!(n-m)!} p^m (1-p)^{n-m} \quad (13)$$

where p is the ratio Al/Si. The probabilities for CAS glasses with C/S = 1.5 and 1.0 are reported in Tables S2 and S3 in Supporting Information. These results endorse that the Al is fully incorporated into the silica network in the simulated amorphous compositions.

Finally, the present force field parameterization was also tested by considering the response of the volumetric properties of the condensed phases to pressure (calculation of the Poisson ratio, bulk, shear and Young moduli). The obtained results are compared in Tables 8 and 9 with results found in the literature for some of the systems (both crystalline and glasses). The errors in elastic constant calculations, which involve deviation from equilibrium conditions, are higher than those found for densities and lattice parameters. However, in this case, errors of 10-15% are considered good results[20] because there is some dispersion of the values even between the published data, evidencing the difficulties involved in this type of experiment, which depends on the number of the defects of the sample, porosity, the technique employed,[59] among other

factors. Thus, it is not surprising the absence of reported mechanical properties for several of the crystalline phases investigated. Even for alite-M_3, the major constituent of cement clinker, the direction-dependent Young moduli were first reported only recently,[23] based on MD results from a force field developed for C_3S. Bearing in mind that our objective is set up a general force field adequate for cement-clinker crystalline and amorphous phases, the results are fairly good. The elastic properties for CS phases are in better agreement with the reported values than the calculated moduli of the CA phases. For alite-M_3 K is underestimated by ca. 15% and G is overvalued by 25%, resulting in the deviation seen in Poisson ratio (we suspect that the same issue is affecting the results for the M_1 polymorph, although there is no experimental data for comparison). This could be corrected in principle by incorporating in the force field a specific descriptor for O_i atoms (present only in this clinker-crystalline phase and in amorphous materials, discussed below) instead of employing a single potential parameter for all oxygen atoms (O_b, O_{nb} and O_i). However, during the melting stage of construction of the amorphous materials the oxygen is able to change its status between O_b, O_{nb} and O_i, and the routine to deal with this task would be computationally expensive.

In comparison to the three-term Buckingham potential, the steeper form of the two-parameter Lennard-Jones potential curve gives rise to more abrupt changes of the ion-pair interaction energy when the interatomic distance r_{ij} departs from equilibrium. Consequently, the moduli calculated with the Lennard-Jones potential are systematically higher than those calculated by the Buckingham potential, as can be seen for Bulk moduli determined through $P \times V$ relationships for crystalline phases with known values of K. On

the other hand the computational cost of the two-parameter model is reduced with respect to the Buckingham potential.

The symmetry of the crystalline phase is related to the number of elastic coefficients.[9] For isotropic materials the Young modulus in the three principal crystal directions are equal. The computed Young moduli in the *x*, *y* and *z* directions for alite-M_1 are ca. 140 GPa and indicate that this polymorph is more isotropic than the M_3 form.[23] The direction-dependent Young moduli are sensible to the changes in the intermediate range order of the materials when going from Ca-rich crystal phase alite (C/S = 3) to wollastonite (C/S = 1). The less compressible directions in belite minerals appears to be associated with more densely packed SiO_4 layers in those directions. The rankinite structure is ordered in successive layers of Ca atoms and Si_2O_7 groups parallel to the *z* direction, with the Si_2O_7 units oriented towards *z* direction and resulting in lower compressibility of the mineral in this direction. In wollastonite minerals the dreierkette-type chains of silica are oriented along the *y* direction and provides higher resistance to compression/expansion with respect to *x* and *z* directions.

The isotropic structure of the C_3A is composed by six-membered rings of AlO_4 tetrahedra, held together by Ca atoms,[11] while the mayenite structure consists of 8-membered rings of AlO_4 tetrahedra interconnected in a cage-like, open framework, resulting in slightly high direction-dependent Young moduli. The crystal structure of krotite consists in layers of six-membered rings of AlO_4 tetrahedra stacked in *y* direction and is more compressible in this direction compared to the *x* and *z* crystal directions. The value of E_x for grossite reveals that the structure is more deformable in the direction of the Ca-rich planes, as well as E_z indicates the same for gehlenite crystal.

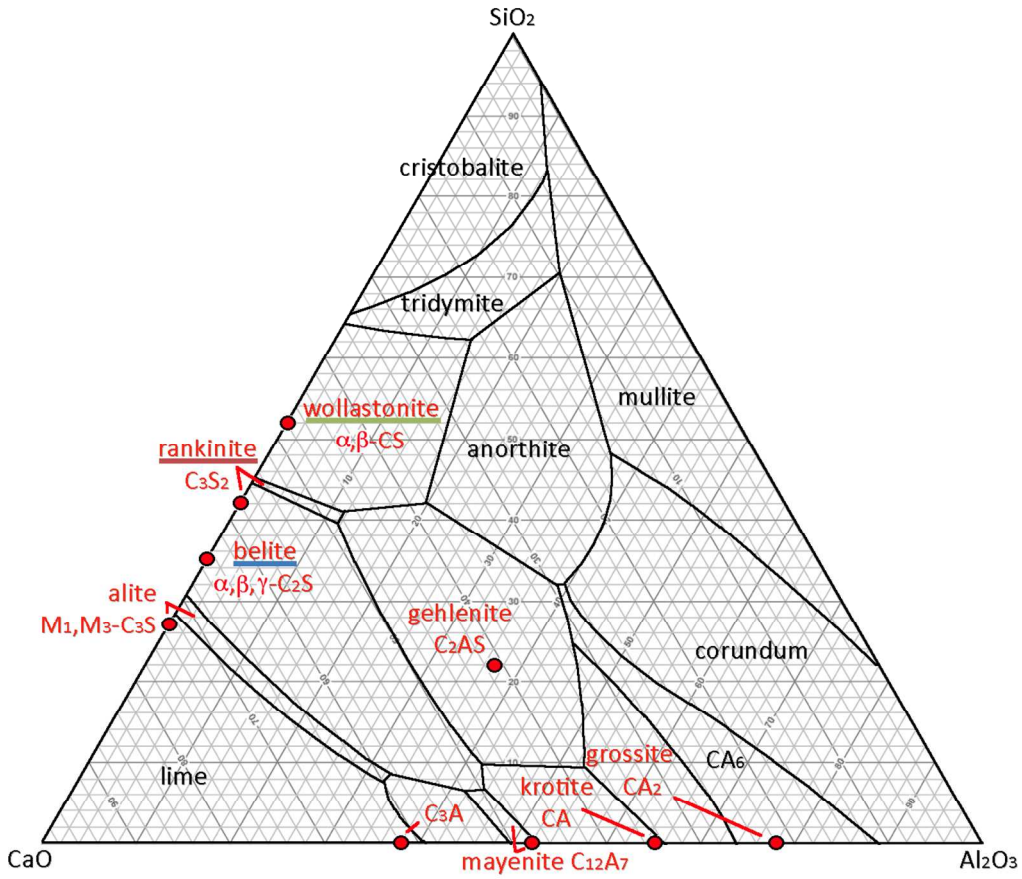

Figure 1. Ternary phase diagram for the CaO-Al_2O_3-SiO_2 system highlighting the different regions where a given oxide component crystallizes from the corresponding melt.[2] Cement notation is given for the different phases that can be present in common cement clinkers, along with the corresponding polymorphs. The labels and points in red correspond to the clinker crystalline phases modeled by the present force-field. Some composition points lie outside the corresponding regions due to the presence of peritectic phase transitions. The colored lines underlining three of the red labels correspond to the color-coding used in figures 2-8, for the three calcium silicate phases more extensively studied in this work.

Table 3. Structural data for selected crystalline phases of the lime-silica-alumina system. Lennard-Jones potential MD data in italic and relative deviations between MD and experimental results in parenthesis. Buckingham potential MD results are given as ESI.

name	**alite**	**alite**	**belite**	**belite**	**belite**	**rankinite**	**wollastonite**	**wollastonite**	–	**mayenite**	**krotite**	**grossite**	**gehlenite**
polymorph	**M_1**	**M_3**	**α**	**β**	**γ**	–	**α**	**β**	–	–	–	–	–
formula	Ca_3SiO_5	Ca_3SiO_5	Ca_2SiO_4	Ca_2SiO_4	Ca_2SiO_4	$Ca_3Si_2O_7$	$CaSiO_3$	$CaSiO_3$	$Ca_3Al_2O_6$	$Ca_{12}Al_{14}O_{33}$	$CaAl_2O_4$	$CaAl_4O_7$	$Ca_2Al_2SiO_7$
CCN	C_3S	C_3S	C_2S	C_2S	C_2S	C_3S_2	CS	CS	C_3A	$C_{12}A_7$	CA	CA_2	C_2AS
space group	*Pc*	*Cm*	*$P6_3mc$*	*$P2_1/n$*	*Pbnm*	*$P2_1/a$*	*P-1*	*$P2_1/a$*	*Pa3*	*I-43d*	*$P2_1/n$*	*C2/c*	*P-42_1 m*
reference	28	29	30	31	32	33	34	35	36	37	38	39	40
MD cells	2×8×5	2×8×3	10×11×8	10×11× 8	10×8×6	5×6×8	7×8×8	4×7×8	4×4×4	5×5×5	6×7×4	4×6×10	7×7×10
MD atoms	12960	15552	12320	13440	11200	11520	13440	13440	16896	14750	14112	11520	11760
a / Å	27.874 *27.918* (0.16)	33.083 *33.305* (0.67)	5.579 *5.623* (0.79)	5.502 *5.637* (2.46)	5.081 *5.118* (0.73)	10.600 *10.652* (0.49)	7.940 *7.866* (-0.93)	15.426 *15.298* (-0.83)	15.263 *15.286* (0.15)	11.979 *12.105* (1.05)	8.700 *8.709* (0.11)	12.840 *13.038* (1.55)	7.690 *7.783* (1.21)
b / Å	7.059 *7.083* (0.34)	7.027 *7.181* (2.19)	5.579 *5.658* (1.42)	6.762 *6.792* (0.43)	11.224 *11.381* (1.39)	8.920 *8.991* (0.79)	7.320 *7.462* (1.94)	7.320 *7.469* (2.03)	15.263 *15.286* (0.15)	11.979 *12.108* (1.08)	8.092 *8.282* (2.35)	8.862 *8.859* (-0.04)	7.690 *7.783* (1.21)
c / Å	12.258 *12.274* (0.13)	18.499 *18.594* (0.52)	7.150 *7.041* (-1.52)	9.339 *9.363* (0.26)	6.778 *6.823* (0.67)	7.890 *8.180* (3.68)	7.070 *7.202* (1.87)	7.066 *7.201* (1.91)	15.263 *15.286* (0.15)	11.979 *12.109* (1.08)	15.191 *15.204* (0.08)	5.431 *5.513* (1.50)	5.100 *5.065* (-0.69)
α / °	90.00 *90.02*	90.00 *90.00*	90.00 *89.98*	90.00 *90.00*	90.00 *90.00*	90.00 *90.00*	90.00 *90.04*	90.00 *90.00*	90.00 *90.00*	90.00 *90.00*	90.00 *90.00*	90.00 *90.00*	90.00 *90.00*
β / °	116.03 *116.06*	94.12 *93.78*	90.00 *90.11*	94.14 *94.85*	90.00 *90.00*	119.60 *120.21*	95.37 *94.45*	95.40 *94.68*	90.00 *90.00*	90.00 *90.03*	90.17 *89.95*	106.83 *105.64*	90.00 *90.00*
γ / °	90.00 *89.98*	90.00 *89.99*	120.00 *120.25*	90.00 *90.00*	90.00 *90.00*	90.00 *90.00*	103.43 *103.64*	90.00 *90.00*	90.00 *90.00*	90.00 *90.05*	90.00 *90.00*	90.00 *90.00*	90.00 *90.00*
V_{cell} / Å^3	2167.24 *2180.43*	4289.43 *4437.13*	192.73 *193.51*	346.55 *357.22*	386.54 *397.43*	648.66 *677.12*	397.82 *409.53*	794.33 *820.05*	3555.66 *3571.54*	1719.12 *1774.76*	1069.45 *1096.69*	591.54 *613.20*	301.59 *306.79*
ρ / g.cm^{-3}	3.150 *3.131* (-0.61)	3.182 *3.096* (-2.69)	3.073 *3.061* (-0.40)	3.301 *3.204* (-2.94)	2.960 *2.880* (-2.72)	2.953 *2.830* (-4.16)	2.909 *2.827* (-2.82)	2.914 *2.824* (-3.10)	3.028 *3.018* (-0.32)	2.690 *2.611* (-3.07)	2.950 *2.873* (-2.46)	2.919 *2.853* (-2.26)	3.019 *2.992* (-0.88)

Table 4. Interatomic distances, r_{ij}, for selected crystalline phases of the lime-silica-alumina system. Comparison between experimental and MD (bold and italic) data.

name	**alite**	**belite**	**rankinite**	**wollastonite**	–	**mayenite**	**krotite**	**grossite**	**gehlenite**
polymorph	**M_3**	**α**	–	**α**	–	–	–	–	–
formula	Ca_3SiO_5	Ca_2SiO_4	$Ca_3Si_2O_7$	$CaSiO_3$	$Ca_3Al_2O_6$	$Ca_{12}Al_{14}O_{33}$	$CaAl_2O_4$	$CaAl_4O_7$	$Ca_2Al_2SiO_7$
CCN	C_3S	C_2S	C_3S_2	CS	C_3A	$C_{12}A_7$	CA	CA_2	C_2AS
MD cells	2×8×3	10×11×8	5×6×8	7×8×8	4×4×4	5×5×5	6×7×4	4×6×10	7×7×10
MD atoms	15552	12320	11520	13440	16896	14750	14112	11520	11760
Os-Oc	0.270-0.310[a]	–	–	–	–	–	–	–	–
	0.305								
Os-Os	0.266[a]	0.258-0.265[c]	0.252-0.276[f]	0.257-0.273[g]	0.286[h]	0.288[i]	0.280[j]	0.283[k]	0.278[l]
	0.260	***0.260***	***0.260***	***0.260***	***0.280***	***0.280***	***0.280***	***0.280***	***0.280***
Ca-O	0.240[a]	0.238-0.242[c]	0.242[f]	0.240[g]	0.234[h]	0.243[i]	0.243[j]	0.248[k]	0.254[l]
	0.243[b]	0.250[d]		0.239[b]					
	0.235-0.240	***0.235-0.240***	***0.240***	***0.240***	***0.240***	***0.240***	***0.240***	***0.240***	***0.245***
Si-O	0.163[a]	0.162-0.164[c]	0.161[f]	0.163[g]	–	–	–	–	0.168[l]
		0.163[d]							
	0.160	***0.160***	***0.160***	***0.160***					***0.160***
Ca-Ca	0.347[b]	0.358-0.375[b]	0.375[f]	0.362[b]	0.315[h]	0.369[i]	0.350[j]	0.434[k]	0.350[l]
		0.350[d]							
		0.363[e]							
	0.330	***0.350***	***0.340***	***0.345***	***0.300***	***0.370***	***0.340***	***0.450***	***0.335***
Al-O	–	–	–	–	0.175[h]	0.175[i]	0.176[j]	0.176[k]	0.175[l]
					0.170	***0.170***	***0.170***	***0.170***	***0.170***

[a]Ref. 41; [b]Ref. 42; [c]Ref. 43; [d]Ref. 44; [e]Ref. 45; [f]Ref. 33; [g]Ref. 46; [h]Ref. 36; [i]Ref. 37; [j]Ref. 47; [k]Ref. 39; [l]Ref. 40

Table 5. MD-calculated and experimental densities, ρ, of amorphous CaO-Al_2O_3-SiO_2 (the name of the crystalline phases with equivalent composition are also given for reference purposes).

Chemical formula	$(CaO)_2(SiO_2)$	$(CaO)_3(SiO_2)_2$	$(CaO)(SiO_2)$	$(CaO)(SiO_2)_2(Al_2O_3)$	$(CaO)(Al_2O_3)$
C/S composition	2/1 (belite)	3/2 (rankinite)	1/1 (wollastonite)	1/2 (anorthite)	– (krotite)
reference		7	7	48 / 49 / 50	49
Atoms /box	9730	9852	9900	9841	10185
ρ_{MD} / g.cm^{-3}	2.965	2.910	2.818	2.649	2.888
ρ_{exp} / g.cm^{-3}	–	2.966	2.880	2.605 / 2.639 / 2.690	2.880

Table 6. Average distances, r_{ij} (in nm), and average coordination numbers in $(CaO)_x(SiO_2)_{1-x}$ glass models. The cutoffs for the coordination shells were the first minima in radial distribution functions ($g_{CaO}(r_{shell})$ = 0.310 nm, $g_{SiO}(r_{shell})$ = 0.185 nm, and $g_{CaCa}(r_{shell})$ = 0.510 nm). Oxygen atoms closer than $g_{SiO}(r_{shell})$ of two Si atoms were classified as bridging oxygens, O_b, closer than $g_{SiO}(r_{shell})$ of only one Si atom are nonbridging oxygens, O_{nb}, and away than $g_{SiO}(r_{shell})$ of any Si atom are isolated oxygens, O_i.

x	r_{SiO}	N_{SiO}	N_{SiOb}	N_{SiOnb}	r_{CaO}	N_{CaO}	N_{CaOb}	N_{CaOnb}	N_{CaOi}	N_{CaCa}
0.67	0.160	4.00	0.40	3.60	0.235	6.36	0.57	5.22	0.57	10.6
0.60	0.160	4.00	0.77	3.23	0.235	6.38	1.18	4.93	0.27	9.30
0.50	0.160	4.00	1.40	2.60	0.235	6.31	2.18	4.05	0.08	7.09
0.5[a]	*0.161*	*4.03*	*2.09*	*1.94*	*0.241*	*6.4*	*1.0*	*5.4*	-	*7.0*
0.50[b]	0.160	4.01	2.00	2.01	0.235	6.3	1.2	5.1	-	7.09

[a]Ref. 6; [b]Data for x = 0.50 analyzed as in Ref. 6.

Table 7. Average distances, r_{ij}/nm, and average coordination numbers in $(CaO)_x(SiO_2)_y(Al_2O_3)_z$ glass models (in mol %). The cutoffs for the coordination shells were the first minima in radial distribution functions ($g_{CaO}(r_{shell})$ = 0.310 nm, $g_{SiO}(r_{shell})$ = 0.185 nm, $g_{AlO}(r_{shell})$ = 0.210 nm and $g_{CaCa}(r_{shell})$ = 0.510 nm). Oxygen atoms closer than $g_{ij}(r_{shell})$ of two network former atoms (Al or Si) were classified as bridging oxygens, O_b, closer than $g_{ij}(r_{shell})$ of only one network former atom are nonbridging oxygens, O_{nb}, and away than $g_{ij}(r_{shell})$ of any network former atom are isolated oxygens, O_i.

CaO	SiO_2	Al_2O_3	r_{AlO}	r_{SiO}	N_{SiO}, N_{AlO}	N_{SiOb}, N_{AlOb}	N_{SiOnb}, N_{AlOnb}	r_{CaO}	N_{CaO}	N_{CaOb}	N_{CaOnb}	N_{CaOi}	N_{CaCa}
58.3	38.8	2.9	0.170	0.160	4.00	1.09	2.91	0.235	6.36	1.68	4.48	0.20	8.76
56.5	37.6	5.9	0.170	0.160	4.00	1.40	2.60	0.235	6.33	2.18	4.02	0.13	8.21
54.6	36.4	9.1	0.170	0.160	4.00	1.71	2.29	0.235	6.32	2.67	3.56	0.09	7.52
48.6	48.6	2.9	0.170	0.160	4.00	1.69	2.31	0.235	6.41	2.68	3.67	0.06	7.01
47.1	47.1	5.9	0.170	0.160	4.00	1.98	2.02	0.235	6.41	3.14	3.21	0.06	6.54
45.5	45.5	9.1	0.170	0.160	4.00	2.23	1.77	0.235	6.28	3.49	2.75	0.04	6.22
25.0	50.0	25.0	0.170	0.160	4.00	3.68	0.32	0.240	6.37	5.85	0.52	0.00	2.29
					3.96	3.64	0.32						
50.0	0	50.0	0.170	-	4.00	3.51	0.49	0.235	6.57	5.77	0.79	0.01	5.36

Table 8. Poisson ratio (ν), bulk (K), shear (G) and Young (E) moduli (in GPa) for selected crystalline phases of the CSA system. Comparison between literature and MD data (in italics).

	Alite-M_1, C_3S	**Alite-M_3, C_3S**[17,23,58,59]	**α-belite, C_2S**[58]	**β-belite, C_2S**[17,58,59,60]
K		105/103[a]/154[b]	161[b]	119[a]/131[a]/111[a]/161[b]
	75.2±1.9	*87.6±2.4/81±4*[c]*/84±2*[d]	*108±5*	*130±1/136±2*[c]*/126±2*[d]
G		54.5[a]		53.1[a]
	62.4±1.6	*67.9±0.8*	*43.5±4.3*	*61.9±0.4*
E		135/147/118/139[a]		130/140/138[a]
	147±3	*162±2*	*115±9*	*160±1*
E_x		152[a]		
	142±5	*158±8*	*105±6*	*177±2*
E_y		176[a]		
	137±7	*158±8*	*117±5*	*239±2*
E_z		103[a]		
	142±1	*145±2*	*120±4*	*203±2*
ν		0.31/0.28		0.30
	0.17	*0.19*	*0.32*	*0.30*
	γ-belite, C_2S[6]	**Rankinite, C_3S_2**[58,61]	**α-wollastonite, CS**[6,58]	**β-wollastonite, CS**
K	114[a]	95[b]	100/115[a]/104	
	103±3/122±1[c]*/109±1*[d]	*106±2/100±1*[c]*/91±1*[d]	120±2/124±1[c]/109±1[d]	*135±2*
G				
	48.3±0.1	*45.5±0.6*	*55.5±0.7*	*65.8±0.6*
E				
	125±1	*119±2*	*144±2*	*170±2*
E_x				
	131±2	*115±2*	*134±1*	*126±1*
E_y				
	59.2±1.3	*118±7*	*214±12*	*270±12*
E_z				
	124±2	*199±7*	*209±10*	*236±6*
ν				
	0.30	*0.31*	*0.30*	*0.29*

	Tricalcium aluminate, C_3A[4,10,27,58,59,11]	**Mayenite, $C_{12}A_7$**[62]	**Krotite, CA**[4,63]	**Grossite, CA_2**[4,58,63]	**Gehlenite, C_2AS**[58,61]
K	106/97[a]/103[a]/98[a]	141[b]/164[e]	86[a]/180[e]	123[a]/194[b]/200[e]	94[b]/108[b]
	134±1/141±2[c]*/124±1*[d]	*122±2/126±1*[c]*/113±2*[d]	*107±1/111±1*[c]*/103±1*[d]	*161±1/174±2*[c]*/132±1*[d]	*165±1/153±2*[c]*/126±1*[d]
G	52.5[a]/54.4[a]				
	65.9±0.6	*56.5±0.3*	*56.4±0.5*	*74.3±0.1*	*77.6±0.7*
E	145/139[a]/134[a]				
	170±2	*147±1*	*144±1*	*193±1*	*201±2*
E_x	160/133[a]				
	162±6	*170±2*	*160±1*	*223±1*	*274±1*
E_y	160/133[a]				
	162±6	*170±2*	*134±2*	*241±1*	*275±1*
E_z	160/133[a]				
	162±6	*170±2*	*151±5*	*272±1*	*159±10*
ν	0.28/0.29				
	0.29	*0.30*	*0.28*	*0.30*	*0.30*

[a]calculated *ab initio* or MD; [b]calculated from thermodynamic and thermoelastic parameters; [c]results from $P\times V$ MD simulations with the Lennard-Jones FF; [d]results from $P\times V$ MD simulations with the Buckingham FF; [e]estimated from the weighted mean between C (111 GPa) and A (255 GPa).

Table 9 Poisson ratio (ν), bulk (K), shear (G) and Young (E) moduli (in GPa) for selected amorphous phases of the CSA system. Comparison between literature and MD data (in italics).

	CS glass[49]	**CA glass**[49]	**CAS_2 glass**[49]	**C_2S glass**	**C_3S_2 glass**
K	69.2	79	69.2		
	73.9±2.5	*109±2*	*91.3±2.5*	*78.7±5.9*	*80.7±2.4*
G	36.3	40.7	38.7		
	37.0±1.2	*53.3±1.0*	*58.0±0.7*	*33.7±1.4*	*32.0±1.6*
E	118	133	121		
	95.1±2.9	*137±3*	*144±2*	*88.4±3.8*	*84.9±3.8*
E_x	92.7	104	98		
	96.6±3.2	*137±2*	*145±4*	*90.2±4.6*	*86.3±3.0*
E_y	92.7	104	98		
	96.6±3.2	*137±2*	*145±4*	*90.2±4.6*	*86.3±3.0*
E_z	92.7	104	98		
	96.6±3.2	*137±2*	*145±4*	*90.2±4.6*	*86.3±3.0*
ν	0.28	0.28	0.26		
	0.29	*0.29*	*0.24*	*0.31*	*0.32*

Crystal structures and amorphous models with composition $(CaO)_x$–$(SiO_2)_{1-x}$.

Figure 2 shows snapshots of the simulation runs for some of the calcium silicate phases studied. There are significant modifications in the structure of the calcium silicate crystals as the ratio C/S changes, related to the spatial distribution of the Ca atoms as well as to the organization of the SiO_x units on the crystals. In alite and belite polymorphs the $[SiO_4]^{4-}$ groups are isolated and present some degree of orientational disorder in the superstructure.[29,64] Also, the inspection of the oxygen atoms in belite reveals that all O are in the vicinity of a Si atom (non-bridging oxygen, O_{nb})[6] whereas in alite polymorphs there is a fraction of interstitial O atoms closer to Ca than to Si, with an ionic character (isolated oxygen, O_i).[65] In the rankinite crystal the Si and O atoms are arranged in sorosilicate groups $[Si_2O_7]^{6-}$ in which a central O connects two SiO_3 units (bridging oxygen, O_b). In wollastonite polymorphs Si and O atoms are arranged in long parallel dreierkette-type chains of $\{[SiO_3]^{2-}\}_n$ units and there is an increase in the number of the bridging oxygen atoms in comparison to rankinite. This structural shifts among the four types of calcium silicate crystals (wollastonite, rankinite, belite and alite) can be summarized using the Q^n terminology, that designates how a given silica tetrahedron is connected to other silica tetrahedra in a given crystal: Q^2 denotes a silica tetrahedron connected to another two tetrahedral units and is the hallmark of wollastonite crystals with their chains of silica tetrahedra (Figure 2a); Q^1 is typical of the sorosilicate groups of rankinite, i.e. isolated pairs of tetrahedrons (Figure 2b); Q^0 represents isolated silicate tetrahedra like those of belite or alite . The difference between these last two crystals lies in the absence (belite, Figures 2c) or presence (alite, Figure 2d) of oxygen atoms not connected to the silicate groups.

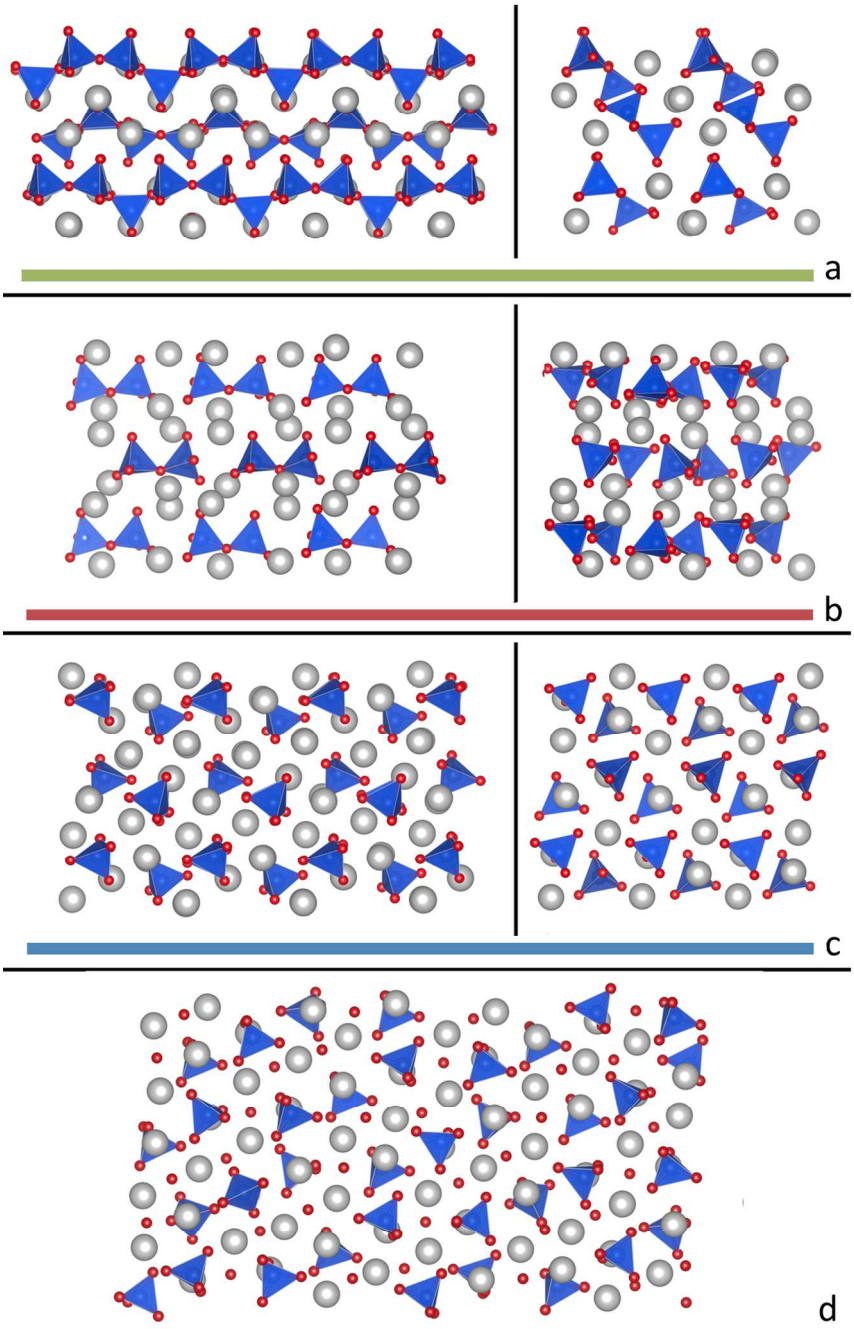

Figure 2. Selected snapshots of equilibrated MD simulation runs of the crystalline structures of: β-wollastonite (green, a); rankinite (red, b); α-belite (blue, c); and alite-M_3 (d). Calcium, silicon and oxygen atoms are depicted as grey, blue and red spheres, respectively. The $[SiO_4]^{4-}$ groups are represented as blue tetrahedra. Images a-c represent side- and top-views of the corresponding crystalline phases.

The most important issue to take notice at this stage is that although the environment of the silicon, calcium and oxygen atoms present in the different crystals is quite diverse, the properties (structure, density) are still predicted with good accuracy after MD equilibration is attained under *N*-*p*-*T* (anisotropic) ensemble conditions using a fairly simple and general force field parameterization (data between parentheses in Table 2).

The good results obtained for the different calcium silicate crystals compelled us to pursue the modeling of amorphous phases (glasses) obtained by the rapid temperature quenching of calcium silicate melts at high temperature (4000-2500 K, cf. Computational Details section). Figure 3 shows selected snapshots of the MD simulation runs after equilibration under *N*-*p*-*T* ensemble conditions at room temperature. The three glasses have the same chemical composition (C/S ratio) of belite, rankinite and wollastonite crystals. As expected, all crystalline structural arrangements are lost in the amorphous phases. The calculated densities of the calcium silicate glasses are lower than the experimental data for rankinite and wollastonite (around 2%, Table 5), a situation analogous to that observed for the crystalline phases. It must be stressed that even without the use of three-body potential terms, the existence of silica tetrahedral units (and the formation of structures made by them) is preserved in all studied glass phases. Moreover, the typical Si-O distances in the simulated amorphous phases (0.160 nm) agree with experimental data: 0.162 nm for calcium silicate glasses ranging from pure amorphous silica to wollastonite-like glasses with a 1:1 C/S ratio.[66]

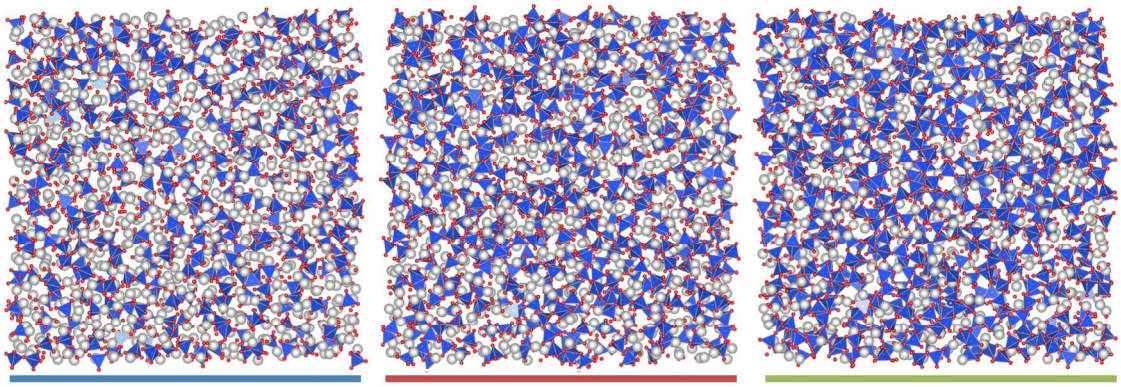

Figure 3. Selected snapshots of equilibrated MD simulation runs (300 K) of three calcium silicate amorphous structures with compositions similar to those of belite (blue, left), rankinite (red, center) and wollastonite (green, right). Calcium, silicon and oxygen atoms are depicted as grey, blue and red spheres, respectively. The $[SiO_4]^{4-}$ groups are represented as blue tetrahedra.

Structure of the modeled calcium silicate phases I: Radial Distribution Functions.

Figures 4 and 5 present the radial distribution functions $g(r_{ij})$ between representative atom pairs in the modeled calcium silicate systems (both crystalline and amorphous phases). Obviously, the variation in the $g(r_{ij})$ functions —peak shifts— among the crystalline polymorphs with the same chemical composition reflects essentially the differences in the arrangement of the atoms within each crystal lattice. On the other hand, the $g(r_{ij})$ functions of the amorphous phases can be understood as an averaged-out function of the most conspicuous peaks in the corresponding crystalline structures.

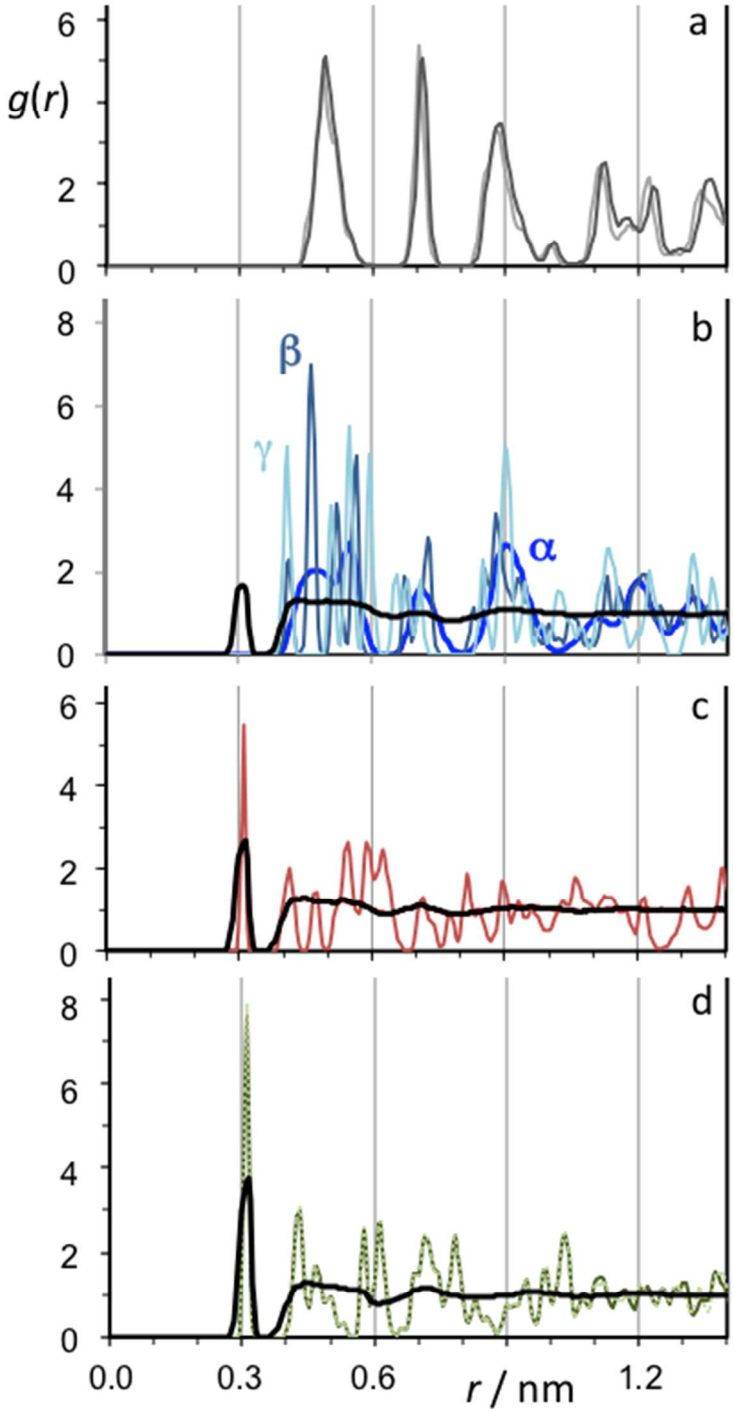

Figure 4. Radial pair distribution functions between the silicon atoms of: M_1 and M_3 alite (light and dark gray, a); α-, β- and γ-belite (labeled blue shades, b); rankinite (red, c) and α- and β-wollastonite (light and dark green, d). The black lines in diagrams a-c represent the corresponding amorphous phases.

The first function to be discussed correlates the characteristic distances between silicon atoms (Si-Si pairs, Figure 4). The four panels of the figure depict $g(r_{SiSi})$ functions that show the progressive destruction of the network of silica tetrahedra as the C/S ratio is increased, from wollastonite to alite. For α- and β-wollastonite and rankinite the first peaks of the crystalline phases appear at around 0.31 nm, indicating silicon atoms connected via a bridging oxygen atom (tetrahedral units joined by one common corner). Such peaks at ca. 0.31 nm are absent in the crystalline forms of alite or belite (only isolated tetrahedral exist in those crystalline forms) but exist for the amorphous phase of belite: there is some degree of silicate di- and trimerization of silica units in belitic glasses.

Figure 4 also shows that the correlations between the silica units are very similar among the different polymorphs of alite (M_1 and M_3, Figure 4a) and wollastonite (α and β, Figure 4d) but quite different among the three polymorphs of belite (α, β and γ, Figure 4b). First, α-belite (the high temperature polymorph of belite) exhibits a $g(r_{SiSi})$ function characterized by broader and less intense peaks than the $g(r_{SiSi})$ functions of the two belite polymorphs (β and γ) found at lower temperatures. This suggests a higher degree of positional freedom within this high temperature polymorph —also reminiscent of the situation found for both high-temperature forms of alite (M_1 and M_3) (Figure 4a). It is interesting to notice that alite (M_1 and M_3) and α-belite are the crystalline phases present in Portland cement clinkers that react more readily with water to yield the C-S-H gel. Second, the difference between the β- and γ-belite polymorphs —both characterized by sharp, intense peaks but with significant shifts between them— seems to indicate that the

isolation of the silica tetrahedral in the calcium oxide matrix caused by a C/S ratio of 2:1 can be accomplished in different ways with concomitantly different degrees of stability.

The second $g(r)$ function to be considered correlates the distances between silicon and oxygen atoms (Si-O pairs, Figure 5). In all cases there are extremely intense and sharp first peaks centered at ca. 0.16 nm, corresponding to the direct binding between the Si and O atoms to form silica units. These agree with the experimentally determined values of 0.162, 0.162 and 0.165 nm for Si–O bond lengths in α-wollastonite, β-wollastonite and γ-belite.[6] Figure 5 also shows a strong secondary peak slightly above 0.4 nm for the crystalline phases of wollastonite (Figure 5d). This corresponds to Si-O distances along the silicate chains found in those crystalline phases. On the other hand the pronounced peaks in Figure 5a (M_1 and M_3 alite), depicted as dotted lines, represent a different class of oxygen atoms (not present at the other C/S compositions), i. e. oxygen atoms that are not bonded to any silicon atom: isolated oxygen atoms. The relative intensity and regular spacing of the peaks reveal i) the relative small proportion of these oxygen atoms (20%); ii) the absence of a contact peak between these oxygen atoms and the silica tetrahedra; and iii) their tendency to be surrounded by calcium atoms.

Finally, if the Ca-O and Ca-Ca pairs are considered (the corresponding $g(r)$ functions are given as supplementary information), one obtains a characteristic Ca-O distance of 0.235 nm for all studied calcium silicate phases (both crystalline and amorphous).

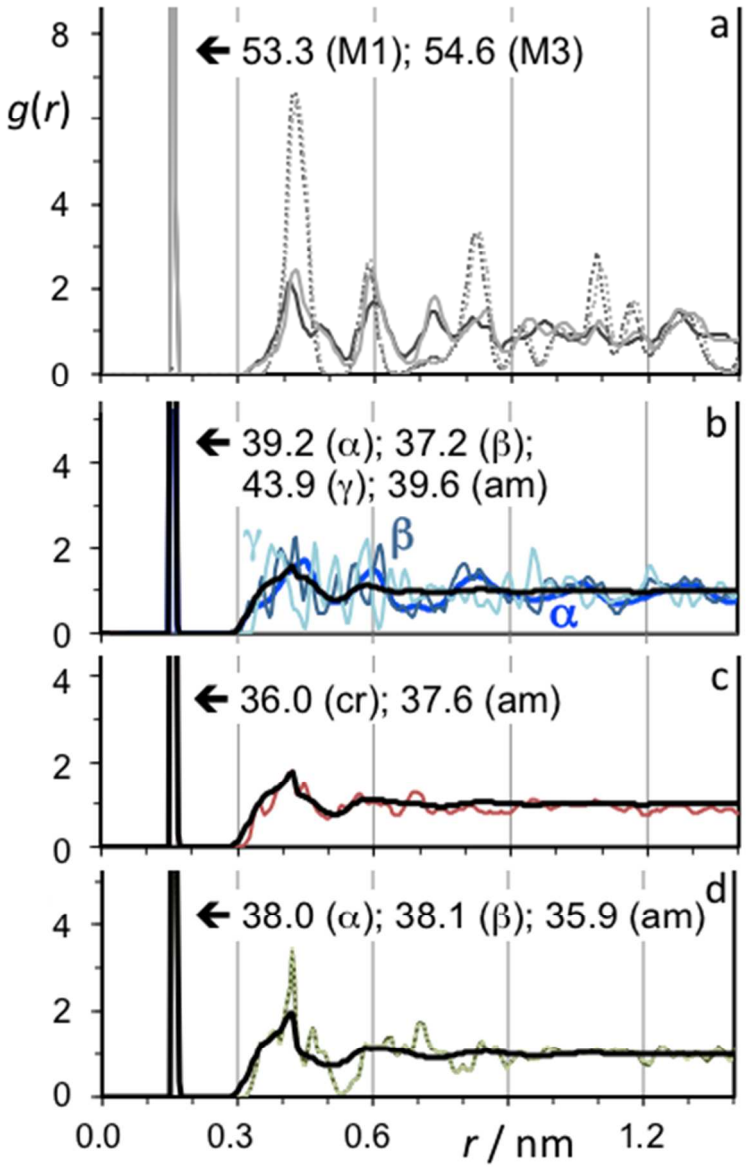

Figure 5. Radial pair distribution functions between the silicon and oxygen atoms of: M_1 and M_3 alite (light and dark gray, a); α-, β- and γ-belite (labeled blue shades, b); rankinite (red, c) and α- and β-wollastonite (light and dark green, d). The black lines in diagrams a-c represent the corresponding amorphous phases. The truncated peaks in all diagrams correspond to the Si-O bonds in the silicate units. The intensities at their maxima are given for each crystalline or amorphous phase.

Structure of the modeled calcium silicate phases II: Aggregate Analyses.

One way to analyze the distribution of silica aggregates in the amorphous calcium silica systems is to calculate the probability of finding a particular atom (Si or O) in a silicate aggregate of size n_a,[67]

$$P(n_a) = \frac{n_a \sum_{j=1}^{C} A_{n_a}(j)}{C \cdot I} \quad (14)$$

where C is the number of configurations sampled in the data production stage, is the number of aggregates of size n_a for a particular configuration j, and I is the total number of atoms (Si + O) in the simulation box.

Figure 6 shows the aggregate size probability distribution functions in amorphous systems with the same C/S ratios of belite, rankinite and wollastonite crystals. In amorphous belite the majority Si and O atoms are covalently bound as isolated silicate tetrahedra (45%), followed by 20% of sorosilicate groups (n_{Si}= 2) and 11% and 7% of clusters with n_{Si}= 3 and 4, respectively. The percentage of unbound oxygen atoms (n_{Si}= 0) is around 7%. Clusters with more than four silicate units represent less than 10% of the total. In amorphous rankinite the cluster distribution is much broader: the number of isolated silica tetrahedra is only 22% and is followed closely by 14%, 8% and 7% of clusters with n_{Si}= 2, 3 and 4 silicate units. The probability of finding larger clusters decreases very slowly, with the 1% mark being attained only for clusters with n_{Si}> 20. Moreover, clusters with sizes varying from n_{Si}= 40 to n_{Si}= 60 can still be found in some of the simulated systems and the number of isolated oxygen atoms is only 3%. Finally, in the case of amorphous wollastonite there is an important structural/morphological shift: the probability of finding small clusters is quite small (6, 3 and 2% for clusters with n_{Si}= 1, 2 and 3, respectively) and decays quite rapidly. On the other hand, the probability of finding silicon atoms in very large aggregates that percolate the entire simulation box

(1600 <n_{Si}< 1700, for the simulated systems with ≈2000 silicon atoms) is very high (84%).

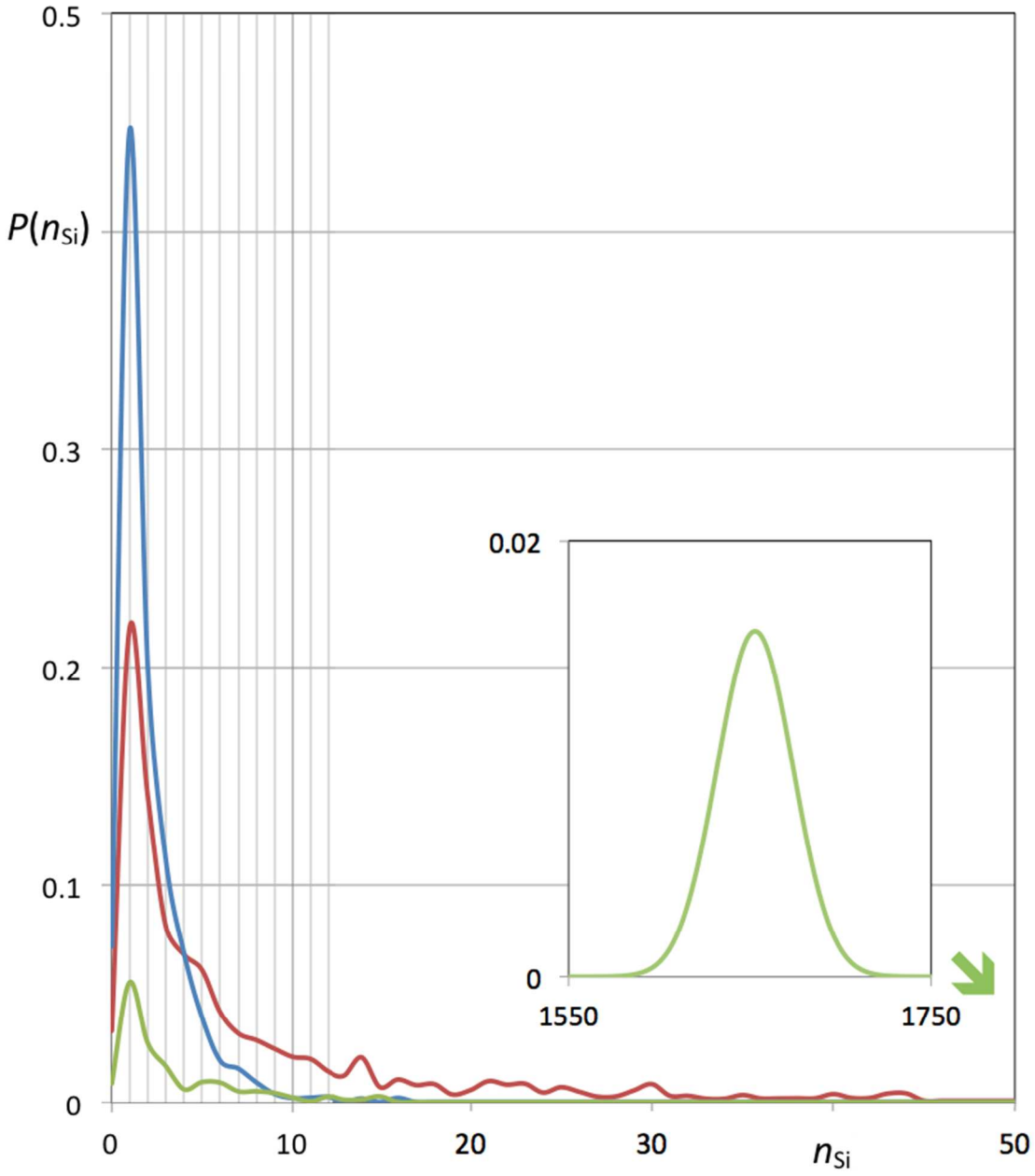

Figure 6. Probability distribution as a function of the number of silicon atoms of a given silicate aggregate for amorphous models of belite (blue), rankinite (red) and wollastonite (green). The inset represents the probability of finding very large aggregates in the wollastonite system. It was scaled 0.1x in the x-axis and 10x in the y-axis relative to the main graph.

The morphology of the amorphous phases can also be discussed in terms of i) the relative amounts of the different types of oxygen atoms (isolated (I), single-bonded (S), and bridging (B)) present in the systems; ii) the Q^n parameters of the tetrahedral units, i. e. the relative amounts of isolated silica tetrahedrons (Q^0), silica units bound by a single oxygen (terminal tetrahedral, Q^1), silica units bound by two oxygen atoms (linear bridging units, Q^2), and silica units bound by three (or even 4) oxygen atoms (branching bridging units, Q^3 and Q^4); and iii) the evaluation of cyclic silica structures in the glassy systems.

Figure 7 shows graphically the first two of those distributions along with three representative simulation snapshots of the amorphous phases, where the different types of silica morphologies are highlighted.

The structural randomization that accompanies each transformation from crystalline to amorphous phase implies that some single-bonded oxygen atoms (that constitute all, 6/7 and 2/3 of the oxygen atoms present in crystalline belite, rankinite and wollastonite, respectively) will either become detached from their silicon atoms and become isolated oxygen atoms, or will form a bond to a second silicon atom and become bridging oxygen atoms. Such dual process is more noticeable in belite (with 9% shifts in each direction), than in rankinite (4% shifts) or in wollastonite (1% shifts). Nevertheless, these sometimes rather modest shifts in terms of types of oxygen atoms, correspond to much larger shifts in terms of the connectivity of the existing silicate units. First it is interesting to notice that belite, rankinite and wollastonite crystals are formed by 100% of Q^0, Q^1 and Q^2 silicate structures, respectively. When glasses with the same C/S ratio are considered, the implicit randomization processes, yield Q^n distributions that still preserve a majority of

the original Q^n type but also contain significant amounts of the other Q types, especially those of type Q^{n+1} or Q^{n-1}.

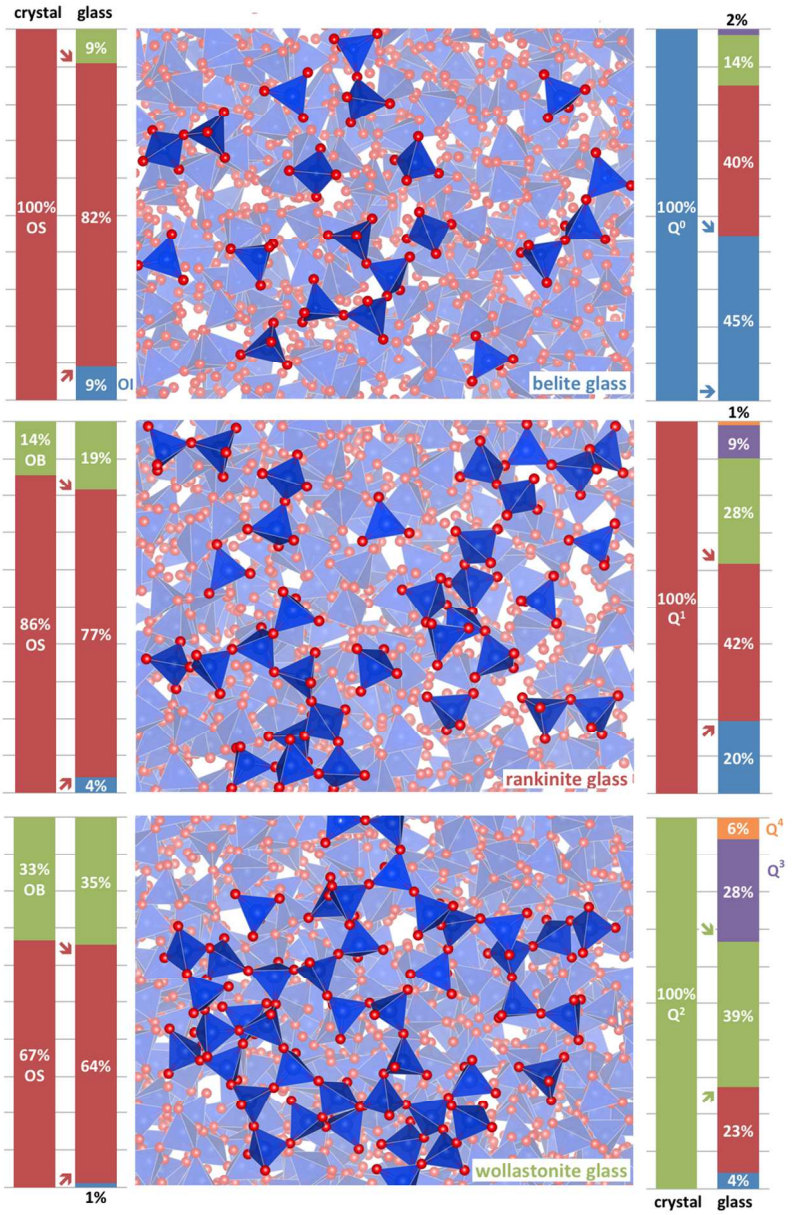

Figure 7. Simulation snapshots of amorphous calcium silicate glasses at T = 300 K: oxygen atoms as red spheres; blue tetrahedra as silicate units; calcium atoms are not represented; selected aggregates are highlighted. The bar-charts on the left represent the relative proportions of isolated (OI, blue) single-bonded (OS, red) and bridging (OB, green) oxygen atoms present in each glass and corresponding crystal. The graphs on the right show the distribution of the silicate units connectivity (Q^0 to Q^4). The arrows indicate distribution shifts from crystal to glass.

When the percentage of Q^2 to Q^4 units in a given system becomes significant (as in the cases of the rankinite and wollastonite glasses) the existence of long chains with possible branching implies the likely formation of cyclic silica structures. The evaluation of such structures (namely the number and size of the rings with fewer members (irreducible) that contain a given silica unit) is an important issue to consider when describing the morphology of three-dimensional aggregates, as those prevalent in silica glasses.[12] Figure 8 depicts the number density and distribution of irreducible rings in amorphous phases of rankinite, wollastonite and pure silica. Amorphous silica is a three dimensional structure composed exclusively of interconnected silica units. Therefore each silica unit can participate simultaneously in different irreducible rings yielding a very high density of irreducible cycles per silica unit (2.65). Moreover, most irreducible rings (almost 80%) have relatively small sizes, between 5 and 7 silica units. The existence of those small and interlocked cyclic structures can be related to the hardness and inertness of silica glasses. In amorphous wollastonite calcium atoms replace half of the silica units present in pure silica glass. Therefore, the original three-dimensional character of the silica network is seriously fragmented and although most of the silica units belong to the same aggregate that percolates the entire simulation box (cf. Figure 6 inset), the different strands must include numerous interruptions (defects) caused by the calcium atoms. This causes a huge decrease in the ring density (from 2.65 to just 0.14) and also a much larger distribution in the size of the irreducible rings (Figure 8). Finally, in the case of rankinite glass one can find small-to-medium sized aggregates (Figure 6) up to sizes of 60 silica units, but no percolating very large aggregates. Most of those medium-sized aggregates

are not branched (p(Q^3)≈ 9%, cf. Figure 8) and do not form cyclic structures. The corresponding ring density is residual, below 0.01.

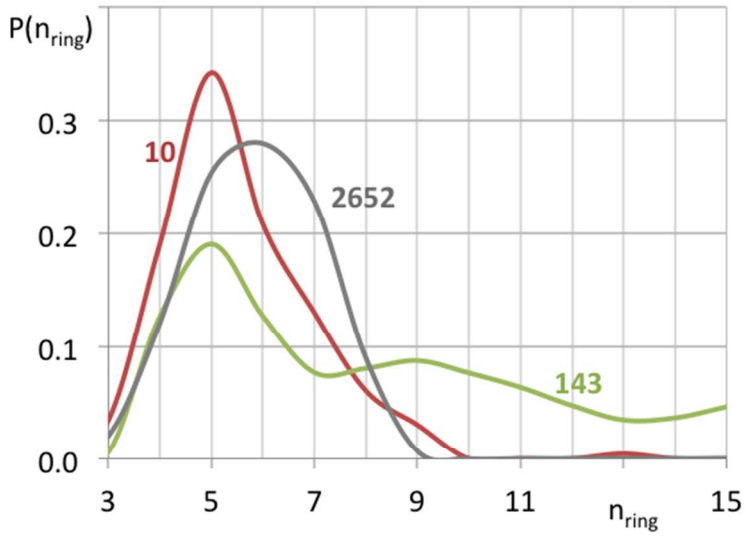

Figure 8. Probability distribution as a function of the number of cyclic silica structures present in the amorphous models of rankinite (red), wollastonite (green), and silica glass (gray). The numbers labeling each curve are the total number of irreducible rings present in each type of glass per 1000 silica units.

Structure of the alumina-doped wollastonite phases

So far the discussion was centered on calcium silicate crystalline and amorphous phases. However, we have developed the present force field parameterization also to include calcium alumina crystalline phases and even gehlenite, a mixed calcium aluminosilicate (C_2AS) crystal (cf. Figure 1). The applicability of the force field to these different structures and the results obtained for the calcium silicate amorphous phases led us to extend our analysis to alumina-doped calcium silicate systems. As mentioned in the introduction, this type of phases are generally present in common Portland cement

clinkers since aluminum (and to a less extent iron) oxides are commonly added to the limestone/clay mixture in order to lower the melting temperature of the mixture and to modify the reactivity properties of the obtained clinker.

In order to test the impact of alumina addition on the structure of calcium silicate amorphous phases, we have focused on what happens when a wollastonite amorphous phase is doped with alumina. Our choice reflects the fact that wollastonite glasses exhibit the most complex and developed silica network (percolating large parts of the corresponding simulation boxes) among the studied calcium silica amorphous phases.

Figure 9 compares the aggregation distribution in the original wollastonite glass (green lines in both Figures 6 and 9) with the corresponding distributions in wollastonite glasses gradually doped with larger amounts of alumina (2.9, 5.9 and 9.1 mol %, purple, cyan and orange lines, respectively). The trend is obvious: as more alumina is added to the structure the size of the large percolating aggregates starts to decrease and the number of smaller aggregates (from isolated silica units to small clusters with $n_{Si} \approx 5$) increases. This is consistent with the partial destruction of the silica network of the wollastonite glass as more alumina "defects" are introduced in the system. It must be stressed that the normal distributions of the larger aggregates were estimated based on the data of just a few (5-6) independent simulation runs, which means that the corresponding Gaussian curves —calculated via aggregate size averages and standard deviations— have some associated degree of uncertainty. Nevertheless, the results show an unambiguous trend towards less extended silica networks as the amount of alumina doping is increased.

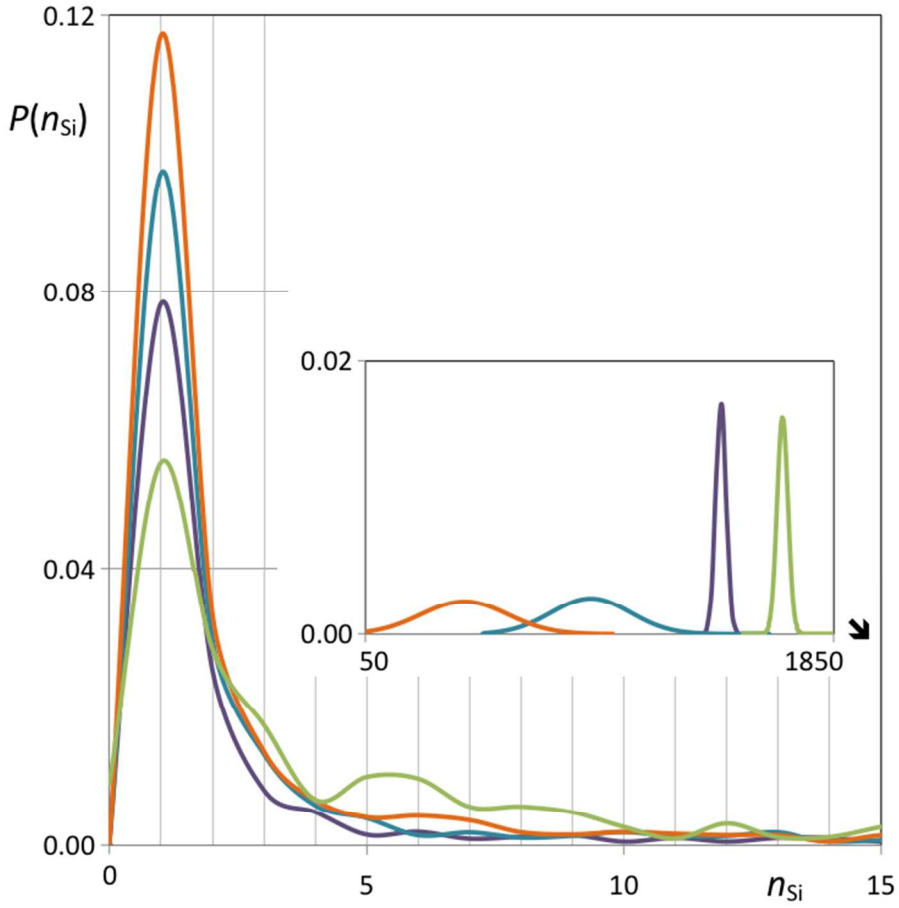

Figure 9. Probability distribution as a function of the number of silicon atoms of a given silicate aggregate for amorphous models of pure wollastonite (green) and wollastonite doped with 2.9 (purple), 5.9 (cyan) and 9.1 mol % (orange) of alumina. The inset represents the probability of finding large aggregates in the wollastonite systems. It was scaled 0.02x in the x-axis and 2x in the y-axis relative to the main graph.

The presence of Al in CAS glass models studied with C/S = 1.5 and C/S = 1.0 induced the formation of oxygen triclusters μ_3, although the quantitites found in the amorphous are rather small. No μ_3 was detected in rankinite-type glasses with up to 2.9 mol % of Al_2O_3, while μ_3 amounts of 0.1% and 0.2% were detected in C_3S_2-like glasses with 5.9 and 9.1 mol % of Al_2O_3, respectively. In C/S = 1 glasses the oxygen tricluster fraction increased from zero in the pure wollastonite glass to 0.02%, 0.1% and 0.3% with 2.9, 5.9

and 9.1 mol % of alumina, respectively. Also, in all cases the major fraction of μ_3 found was OAl_2Si triclusters, followed by OAl_3 triclusters. The occurrence of isolated oxygen atoms O_i decreases with the increase of the Al content. In glasses with C/S = 1.5, O_i is reduced from 4 % in pure C_3S_2 amorphous to ca. 1% in the rankinite glass with 5.9 mol % of alumina. In wollastonite glasses, O_i is lowered to ca. 0.5 % when the Al_2O_3 content is increased to 5.9 mol %. Regarding the overcoordinated species $^{[5]}$Al, trace amounts of 0.04% appeared only in wollastonite-type glasses with compositions of 5.9 and 9.1 mol % of Al_2O_3, suggesting that $^{[5]}$Al plays a minor role as network modifier in the studied CAS amorphous phases. With respect to the silica/alumina network topology, the combined results from MD simulations and the statistical distribution of $Q^n(m\text{Al})$ units given by the Loewenstein's rule pointed out a decrease in Q^1 sites and an increase in high-order Q^n groups, namely Q^2 and Q^3 units in amorphous materials with C/S = 1.5. In C/S = 1 glasses Q^3 species increased at the expense of low Q^n units. The replacement of low Q^n groups by centers with high $Q^n(m\text{Al})$ values leads to a reduction in the number of O_{nb}, increasing the network stability of the amorphous phases. Also, low concentration of O_{nb} sites is associated with the stability of glasses against reaction with water, corrosion and diffusivity. On the other hand, the incorporation of alumina in these amorphous materials introduces new sites for hydrolysis reactions, as the number of the Al-O-Si and Al-O-Al linkages increase.

Conclusions

The present work has shown for the first time that a simple and general force-field based solely on a interionic potential with just two non-bonded interactions terms plus one electrostatic term is capable to capture the most conspicuous structural and elastic

features of different crystalline and amorphous phases present in a wide region of the the lime-alumina-silica diagram.

The eight studied calcium silicate crystalline phases (alite, belite, rankinite, wollastonite and corresponding polymorphs) exhibit striking differences in the arrangement of their silica units within the crystalline lattices (from pure Q^0 connectivity in alite and belite to Q^1 in rankinite and Q^2 in wollastonite) that are well modeled during the MD simulation of each phase using the new general force-field parameterization. Moreover, the generated radial distribution functions revealed that in the case of belite the three studied crystalline forms are quite distinct from each other whereas in the cases of alite and wollastonite such differences are much less pronounced.

The use of a general simple force field also allowed the direct comparison between the structures of a given crystalline phase and the corresponding glass obtained by the rapid quench of the high-temperature melt. The calculated radial distribution functions clearly show the existence of silica clusters in all simulated glasses. The distribution and connectivity of those clusters is highly dependent on the C/S ratio of each cluster and a detailed and novel aggregate analysis revealed that, in the case of wollastonite, a silica network containing most of the silica units present in the glass permeates the entire system.

Finally the parameter transferability between calcium-silicate and calcium-aluminate systems allowed us to perform simulations in wollastonite glasses doped with alumina. The results show that the silica network present in pure wollastonite glass is partially destroyed by the inclusion of alumina “defects”.

The knowledge at an atomistic level of the structure of the silica network in lime-silica-alumina systems and the ways it can be modified in amorphous materials or by the inclusion of other structural units such as alumina is of vital importance for the future formulation of new cement-clinker phases.

Acknowledgements

The authors acknowledge CIMPOR - Cimentos de Portugal, SGPS S.A. for financial support (Industrial Contract adIST/CIMPOR Nanocement 2012/2015).

Supporting Information Available. Table with the MD results for the Buckingham potentials; statistical distribution of $Q^n(m\text{Al})$ units in amorphous with ratios C/S = 1.5 and 1.0 according to the Loewenstein's rule; radial pair distribution functions for Ca-O and Ca-Ca in crystalline alite, belite, rankinite and wollastonite and in amorphous phases with equivalent chemical composition of belite, rankinite and wollastonite.

References

1. Chatterjee, A. K., High belite cements —Present status and future technological options: Part I. *Cem. Concr. Res.* **1996**, *26*, 1213–1225.

2. Taylor, H. F. W. *Cement Chemistry*, 2nd Ed., Thomas Telford Publishing, London, UK, 1997.

3. Cormack, R.; Du, J. Molecular dynamics simulations of soda-lime-silicate glasses. *J. Non-Cryst. Solids* **2001**, *293–295*, 283–289.

4. Thomas, B. W. M.; Mead. R. N. Mountjoy, G. A molecular dynamics study of the atomic structure of $(CaO)_x(Al_2O_3)_{1-x}$ glass with $x = 0.625$ close to the eutectic. *J. Phys. Condens. Matter* **2006**, *18*, 4697–4708.

5. Downs, R. T.; Hall-Wallace, M. The American Mineralogist Crystal Structure Database. *Am. Mineral.* **2003**, *88*, 247–250.

6. Mead, R. N.; Mountjoy, G. A Molecular dynamics study of the atomic structure of $(CaO)_x(SiO_2)_{1-x}$ glasses. *J. Phys. Chem. B* **2006**, *110*, 14273–14278.

7. Doweidar. H. Density-structure correlations in silicate glasses. *J. Non-Cryst. Solids* **1999**, *249*, 194–200.

8. Shimizu, K.; Pensado, A.; Malfreyt, P.; Pádua, A. A. H.; Canongia Lopes, J. N. 2D or not 2D: Structural and charge ordering at the solid-liquid interface of the 1-(2-hydroxyethyl)-3-methylimidazolium tetrafluoroborate ionic liquid. *Faraday Discuss.* **2012**, *154*, 155–169.

9. Saad, M. *Elasticity Theory, applications, and numerics*, Elsevier Butterworth-Heinermann, Oxford, UK, 2005.

10. Moon, J.; Yoon, S.; Wentzcovitch, R. M.; Clark, S. M.; Monteiro, P. J. M. Elastic properties of tricalcium aluminate from high-pressure experiments and first-principles calculations. *J. Am. Ceram. Soc.* **2012**, *95*, 2972–2978.

11. Manzano, H.; Dolado, J. S.; Ayuela, A. Structural, mechanical, and reactivity properties of tricalcium aluminate using first-principles calculations. *J. Am. Ceram. Soc.* **2009**, *92*, 897−902.

12. Le Roux, S.; Jund, P. Ring statistics analysis of topological networks: New approach and application to amorphous GeS_2 and SiO_2 systems. *Comput. Mater. Sci.* **2010**, *49*, 70–83.

13. Guttman, L. Ring structure of the crystalline and amorphous forms of silicon dioxide. *J. Non-Cryst. Solids* **1990**, *116*, 145–147.

14. Momma K.; Izumi, F. VESTA 3 for three-dimensional visualization of crystal, volumetric and morphology data. *J. Appl. Crystallogr.* **2011**, *44*, 1272−1276.

15. Grey, T.; Gale, J.; Nicholson, D.; Artacho, E.; Soler, J. In *A computational exploration of cation locations in high-silica Ca-Chabazite*; Unger, K. K., Kreysa, G., Baselt, J. P., Eds.; Studies in Surface Science and Catalysis 128; Elsevier Science: Amsterdan, Netherlands, 2000; pp 89–98.

16. Kundu, T. K.; Rao, K. H.; Parker, S. C. Competitive adsorption on wollastonite: an atomistic simulation approach. *J. Phys. Chem. B* **2005**, *109*, 11286−11295.

17. Manzano, H.; Dolado, J. S.; Ayuela, A. Elastic properties of the main species present in Portland cement pastes. *Acta Mater.* **2009**, *57*, 1666–1674.

18. Manzano, H.; Durgun, E.; Qomi, M. J. A.; Ulm, F.-J.; Pellenq, R. J. M.; Grossman, J. C. Impact of chemical impurities on the crystalline cement clinker phases determined by atomistic simulations. *Cryst. Growth Des.* **2011**, *11*, 2964–2972.

19. Manzano, H.; Moeini, S.; Marinelli, F.; van Duin, A. C. T.; Ulm, F.-J.; Pellenq, R. J. M. Confined water dissociation in microporous defective silicates: mechanism, dipole

distribution, and impact on substrate properties. *J. Am. Chem. Soc.* **2012**, *134*, 2208−2215.

20. Pedone, A.; Malavasi, G.; Menziani, M. C.; Cormack, A. N.; Segre, U. A new self-consistent empirical interatomic potential model for oxides, silicates, and silica-based glasses. *J. Phys. Chem. B* **2006**, *110*, 11780−11795.

21. Freeman, C. L.; Harding, J. H.; Cooke, D. J.; Elliott, J. A.; Lardge, J. S.; Duffy, D. M. New force fields for modeling biomineralization processes. *J. Phys. Chem. C* **2007**, *111*, 11943−11951.

22. Qomi, M. J. A.; Krakowiak, K. J.; Bauchy, M.; Stewart, K. L.; Shahsavari, R.; Jagannathan, D.; Brommer, D. B.; Baronnet, A.; Buehler, M. J.; Yip, S.; Ulm, F.-J.; Van Vliet, K. J.; Pellenq, R. J.-M. Combinatorial molecular optimization of cement hydrates. *Nat. Commun.* **2014**, *5*, 4960.

23. Mishra, R. K.; Flatt, R. J.; Heinz, H. Force field for tricalcium silicate and insight into nanoscale properties: cleavage, initial hydration and adsorption of organic molecules. *J. Phys. Chem. C* **2013**, *117*, 10417−10432.

24. Nevins, D.; Spera, F. J. Molecular dynamics simulations of molten $CaAl_2Si_2O_8$: dependence of structure and properties on pressure. *Am. Mineral.* **1998**, *83*, 1220–1230.

25. Cygan, R. T.; Liang, J.-J.; Kalinichev, A. G. Molecular models of hydroxide, oxyhydroxide, and clay Phases and the development of a general force field. *J. Phys. Chem. B* **2004**, *108*, 1255–1266.

26. Heinz, H.; Lin, T.-J.; Mishra, R. K.; Emami, F. S. Thermodynamically consistent force fields for the assembly of inorganic, organic, and biological nanostructures: the INTERFACE force field. *Langmuir* **2013**, *29*, 1754−1765.

27. Mishra, R. K.; Fernández-Carrasco, L.; Flatt, R. J.; Heinz, H. A force field for tricalcium aluminate to characterize surface properties, initial hydration, and organically modified interfaces in atomic resolution. *Dalton Trans.* **2014**, *43*, 10602–10616.

28. de Noirfontaine, M.-N.; Courtial, M.; Dunstetter, F.; Gasecki, G.; Signes-Frehel, M. Tricalcium silicate Ca_3SiO_5 superstructure analysis: a route towards the structure of the M_1 polymorph. *Z. Kristallogr.* **2012**, *227*, 102–112.

29 . Nishi, F.; Takeuchi, Y. Tricalcium silicate $Ca_3O[SiO_4]$: The monoclinic superstructure. *Z. Kristallogr.* **1985**, *172*, 297–314.

30. Udagawa, S.; Urabe, K.; Yano, T.; Stabilisation mechanism of polymorphisms of Ca_2SiO_4, Rev. 34th General Meeting, Cement Association of Japan, Tokyo (1980), 37–39.

31. Tsurumi, T; Hirano, Y; Kato, H; Kamiya, T; Daimon, M. Crystal structure and hydration of belite. *Ceram. Trans.* **1994**, *40*, 19–25.

32. Udagawa, S.; Urabe, K.; Natsume, M.; Yano, T. Refinement of the crystal structure of γ-Ca_2SiO_4. *Cem. Concr. Res.* **1980**, *10*, 139–144.

33. Kusachi, I.; Henmi, C.; Kawahara, A.; Henmi, K. The structure of rankinite. *Mineralogical J.* **1975**, *8*, 38–47.

34. Ito, T.; Sadanaga, R.; Takeuchi, Y.; Tokonami, M. The existence of partial mirrors in wollastonite. *Proc. Jpn. Acad.* **1969**, *45*, 913–918.

35. Trojer, F. J. The crystal structure of parawollastonite. *Z. Kristallogr.* **1968**, *127*, 291–308.

36. Mondal, P.; Jeffery, J. The crystal structure of tricalcium aluminate, $Ca_3Al_2O_6$. *Acta Crystallogr. Sect. B-Struct. Sci.* **1975**, *31*, 689–697.

37. Boysen, H.; Lerch, M.; Stys, A.; Senyshyn, A. Structure and oxygen mobility in mayenite ($Ca_{12}Al_{14}O_{33}$): a high-temperature neutron powder diffraction study. *Acta Crystallogr. Sect. B-Struct. Sci.* **2007**, *63*, 675–682.

38. Horkner, W.; Muller-Buschbaum, H. Zur kristallstruktur von $CaAl_2O_4$. *J. Inorg. Nucl. Chem.* **1976**, 38, 983–984.

39. Goodwin, D. W.; Lindop, A. J. The crystal structure of $CaO.2Al_2O_3$. *Acta Crystallogr. Sect. B-Struct. Sci.* **1970**, *26*, 1230–1235.

40. Swainson, I. P.; Dove, M. T.; Schmahl, W. W.; Putnis, A. Neutron powder diffraction study of the akermanite-gehlenite solid solution series. *Phys. Chem. Miner.* **1992**, *19*, 185–195.

41. De La Torre, A. G.; Bruque, S.; Campo, J.; Aranda, M. A. G. The superstructure of C_3S from synchrotron and neutron powder diffraction and its role in quantitative phase analyses. *Cem. Concr. Res.* **2002**, *32*, 1347–1356.

42. Jost, K. H.; Ziemer, B.; Seydel, R. Redetermination of the Structure of β-Dicalcium Silicate. *Acta Crystallogr. Sect. B-Struct. Sci.* **1977**, *33*, 1696–1700.

43. Barbier, J.; Hyde, B. G. The Structures of the Polymorphs of Dicalcium Silicate, Ca_2SiO_4. *Acta Crystallogr. Sect. B-Struct. Sci.* **1985**, *41*, 383–390.

44. Yamnova, N. A.; Zubkova, N. V.; Eremin, N. N.; Zadov, A. E.; Gazeev, V. M. Crystal Structure of Larnite β-Ca_2SiO_4 and Specific Features of Polymorphic Transitions in Dicalcium Orthosilicate. *Crystallogr. Rep.*, **2011**, *56*, 210–220.

45. Gobechiya, E. R.; Yamnova, N. A.; Zadov, A. E.; Gazeev, V. M. Calcio-Olivine γ-Ca_2SiO_4: I. Rietveld Refinement of the Crystal Structure. *Crystallogr. Rep.*, **2008**, *53*, 404–408.

46 . Hesse, H. F. Refinement of the crystal structure of wollastonite-2M (parawollastonite). *Z. Kristallogr.* **1984**, *168*, 93–98.

47. Ma, C.; Kampf, A. R.; Connolly Jr., H. C.; Beckett, J. R.; Rossman, G. R.; Smith, S. A. S.; Schrader, D. L. Krotite, $CaAl_2O_4$, a new refractory mineral from the NWA 1934 meteorite. *Am. Mineral.* **2011**, *96*, 709–715.

48. Petkov, V.; Gerber, T.; Himmel, B. Atomic ordering in $Ca_{x/2}Al_xSi_{1-x}O_2$ glasses (x = 0, 0.34, 0.5, 0.68) by energy-dispersive x-ray diffraction. *Phys. Rev. B* **1998**, *58*, 11982–11989.

49. Haeri, A. Y.-; Ho, C. T.; Weber, R.; Diefenbacher, J.; McMillan, P. F. Elastic properties of aluminate glasses via Brillouin spectroscopy. *J. Non-Cryst. Solids* **1998**, *241*, 200–203.

50. Neuville, D. R.; Cormier, L.; Massiot, D. Al environment in tectosilicate and peraluminous glasses: a ^{27}Al MQ-MAS NMR, Raman, and XANES investigation. *Geochim. Cosmochim. Acta* **2004**, *68*, 5071–5079.

51. Mei, Q.; Benmore, C. J.; Siewenie, J.; Weber, J. K. R.; Wilding, M. Diffraction study of calcium aluminate glasses and melts: I. High energy x-ray and neutron diffraction on glasses around the eutectic composition. *J. Phys.: Condens. Matter* **2008**, *20*, 245106.

52. Neuville, D. R.; Cormier, L.; Massiot, D. Al coordination and speciation in calcium aluminosilicate glasses: effects of composition determined by ^{27}Al MQ-MAS NMR and Raman spectroscopy. *Chem. Geol.* **2006**, *229*, 173–185.

53. Stebbins, J. F.; Xu, Z. NMR evidence for excess non-bridging oxygen in an aluminosilicate glass. *Nature* **1997**, *390*, 60–62.

54. Akola, J.; Kohara, S.; Ohara, K.; Fujiwara, A.; Watanabe, Y.; Masuno, A.; Usuki, T.; Kubo, T.; Nakahira, A.; Nitta, K.; Uruga, T.; Weber, J. K. R.; Benmore, C. J. Network topology for the formation of solvated electrons in binary $CaO–Al_2O_3$ composition glasses. *Proc. Natl. Acad. Sci. U.S.A.* **2013**, *110*, 10129–10134.

55. Iuga, D.; Morais, C.; Gan, Z.; Neuville, D. R.; Cormier, L.; Massiot, D. NMR heteronuclear correlation between quadrupolar nuclei in solids. *J. Am. Chem. Soc.* **2005**, *127*, 11540–11541.

56. Bouhadja, M.; Jakse, N.; Pasturel, A. Striking role of non-bridging oxygen on glass transition temperature of calcium aluminosilicate glass-formers. *J. Chem. Phys.* **2014**, *140*, 234507.

57 . Leonelli, C.; Lusvardi, G.; Montorsi, M.; Menziani, M. C.; Menabue, L.; Mustarelli, P.; Linati, L. Influence of small additions of Al_2O_3 on the properties of the $Na_2O{\cdot}3SiO_2$ glass. *J. Phys. Chem. B* **2001**, *105*, 919–927.

58. Ottonello, G.; Attene, M.; Ameglio, D.; Belmonte, D.; Zuccolini, M. V.; Natali, M. Thermodynamic investigation of the $CaO–Al_2O_3–SiO_2$ system at high *P* and *T* through polymer chemistry and convex-hull techniques. *Chem. Geol.* **2013**, *346*, 81–92.

59. Velez, K.; Maximilien, S.; Damidot, D.; Fantozzi, G.; Sorrentino, F. Determination by nanoindentation of elastic modulus and hardness of pure constituents of Portland cement clinker. *Cem. Concr. Res.* **2001**, *31*, 555–561.

60 . Mead, R. N.; Mountjoy, G. A molecular dynamics study of densification mechanisms in calcium silicate glasses $CaSi_2O_5$ and $CaSiO_3$ at pressures of 5 and 10 GPa. *J. Chem. Phys.* **2006**, *125*, 154501.

61. Holland, T. J . B.; Powell, R. An internally consistent thermodynamic data set for phases of petrological interest. *J. Metamorphic Geol.* **1998**, *16*, 309–343.

62. Zhang, X.; Wang, Y.; Wang, H.; Cui, Q.; Wang, C.; Ma, Y.; Zou, G. Pressure-induced amorphization in mayenite ($12CaO{\cdot}7Al_2O_3$). *J. Chem. Phys.* **2011**, *135*, 094506.

63 . Hofmeister, A. M. Physical properties of calcium aluminates from vibrational spectroscopy. *Geochim. Cosmochim. Acta* **2004**, *68*, 4721–4726.

64. Dunstetter, F.; de Noirfontaine, M.-N.; Courtial, M. Polymorphism of tricalcium silicate, the major compound of Portland cement clinker 1. Structural data: review and unified analysis. *Cem. Concr. Res.* **2006**, *36*, 39–53.

65. Durgun, E.; Manzano, H.; Pellenq, R. J. M.; Grossman, J. C. Understanding and controlling the reactivity of the calcium silicate phases from First Principles. *Chem. Mater.* **2012**, *24*, 1262−1267.

66. Taniguchi, T.; Okuno, M.; Matsumoto, T. X-ray diffraction and EXAFS studies of silicate glasses containing Mg, Ca and Ba atoms. *J. Non-Cryst. Solids* **1997**, *211*, 56–63.

67. Shimizu, K.; Bernardes, C. E. S.; Canongia Lopes, J. N. Structure and aggregation in the 1‑alkyl-3-methylimidazolium bis(trifluoromethylsulfonyl)imide ionic liquid homologous series. *J. Phys. Chem. B* **2014**, *118*, 567−576.

TOC:

Probing the Lime-Silica-Alumina Diagram using MD Simulations with a Simple and Systematic Forcefield: From Crystalline to Amorphous Phases.

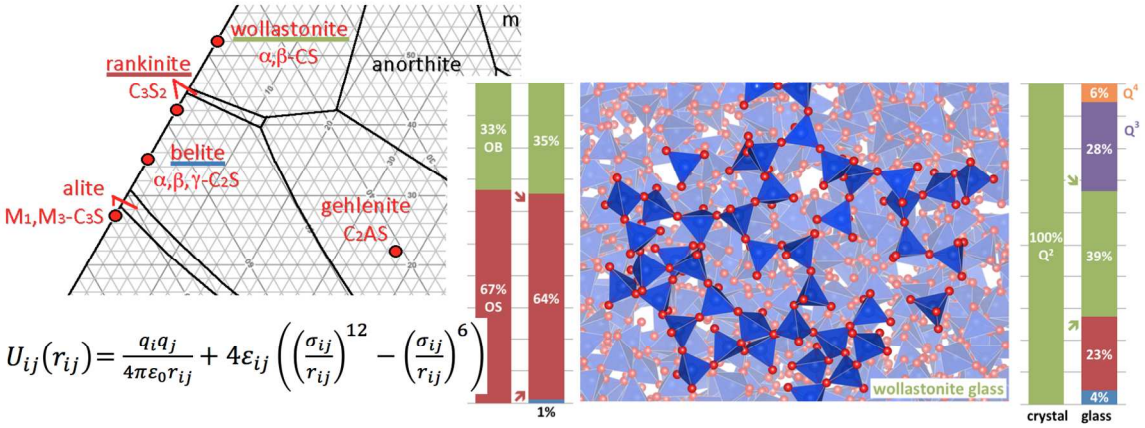

$$U_{ij}(r_{ij}) = \frac{q_i q_j}{4\pi\varepsilon_0 r_{ij}} + 4\varepsilon_{ij}\left(\left(\frac{\sigma_{ij}}{r_{ij}}\right)^{12} - \left(\frac{\sigma_{ij}}{r_{ij}}\right)^{6}\right)$$